# Region-based adaptive anisotropic diffusion for image enhancement and denoising

**Yi Wang**
**Ruiqing Niu**
China University of Geosciences
Institute of Geophysics and Geomatics
Lumo Road 388
Wuhan, Hubei 430074, China
E-mail: wangyi@whu.edu.cn

**Liangpei Zhang**
Wuhan University
State Key Laboratory of Information Engineering in Surveying, Mapping, and Remote Sensing
129 Luoyu Road
Wuhan, Hubei 430079, China

**Huanfeng Shen**
Wuhan University
School of Resource and Environmental Science
129 Luoyu Road
Wuhan, Hubei 430079, China

**Abstract.** A novel region-based adaptive anisotropic diffusion (RAAD) is presented for image enhancement and denoising. The main idea of this algorithm is to perform the region-based adaptive segmentation. To this end, we use the eigenvalue difference of the structure tensor of each pixel to classify an image into homogeneous detail, and edge regions. According to the different types of regions, a variable weight is incorporated into the anisotropic diffusion partial differential equation for compromising the forward and backward diffusion, so that our algorithm can adaptively encourage strong smoothing in homogeneous regions and suitable sharpening in detail and edge regions. Furthermore, we present an adaptive gradient threshold selection strategy. We suggest that the optimal gradient threshold should be estimated as the mean of local intensity differences on the homogeneous regions. In addition, we modify the anisotropic diffusion discrete scheme by taking into account edge orientations. We believe our algorithm to be a novel mechanism for image enhancement and denoising. Qualitative experiments, based on various general digital images and several T1- and T2-weighted magnetic resonance simulated images, show significant improvements when the RAAD algorithm is used versus the existing anisotropic diffusion and the previous forward and backward diffusion algorithms for enhancing edge features and improving image contrast. Quantitative analyses, based on peak signal-to-noise ratio, the universal image quality index, and the structural similarity confirm the superiority of the proposed algorithm. © *2010 Society of Photo-Optical Instrumentation Engineers.* [DOI: 10.1117/1.3517741]

Subject terms: anisotropic diffusion; adaptive; forward and backward; region based; image enhancement; image denoising.

Paper 100468RR received Jun. 9, 2010; revised manuscript received Sep. 25, 2010; accepted for publication Sep. 29, 2010; published online Nov. 30, 2010.

## 1 Introduction

Images taken with both digital cameras and conventional film cameras will pick up noise from a variety of sources, such as different illumination conditions, image quantization, compression, transmission, etc. These sources of image degradation normally arise during image acquisition and processing and have a direct bearing on the visual quality of the image.[1] Undoing these imperfections to remove the image degradation is crucial for aesthetic purposes as in artistic work or marketing, or for practical purposes, such as computer vision. Of particular interest to this study is the work related to image enhancement and denoising that aims to improve signal-to-noise ratio (SNR) and contrast-to-noise ratio (CNR).[2–7]

The scale-space concept was first presented by Iijima[8,9] and Weickert et al.[10] and became popular later on by the works of Witkin[11] and Koenderink.[12] The theory of linear scale-space supports edge detection and localization, while suppressing noise by tracking features across multiple scales.[11–16] In fact, the linear scale space is equivalent to a linear heat diffusion equation.[12,13] However, this equation was found to be problematic in that all edge features are smeared and distorted after a few iterations of linear diffusion. In order to remedy the difficulties encountered in the linear scale-space theory, Perona and Malik[17] developed an adaptive smoothing and edge-detection scheme in which they replaced the linear heat diffusion equation by a selective diffusion that preserves edges. Since its first formulation developed by Perona and Malik,[17] anisotropic diffusion has received a great deal of attention and experienced significant advances, with promising results and applications in many specific domains.[18–46] The main motivation for anisotropic diffusion is to reduce noise while minimizing image blurring across boundaries, but this process does have several drawbacks, including the fact that fine structures in low SNR or CNR regions often disappear and increased blurring occurs in fuzzy boundaries. In our earlier work,[43] we proposed a local variance-controlled forward-and-backward (LVCFAB) diffusion scheme in context of image enhancement and noise reduction. In this scheme, spatial gradient and contextual discontinuity of a pixel are jointly employed for controlling during the evolution. However, a solution to estimating the contextual discontinuity leads to an exhaustive search procedure, which causes algorithm complexity to be too costly. Furthermore, an optimal strategy for evaluating the two gradient thresholds in the forward-and-backward (FAB) diffusion scheme is unknown and, hence, it is often necessary to select the thresholds by guesswork. However, the thresholds vary from image to image and even from region to region within an image. Recently, we presented a tunable FAB (TFAB) diffusion approach for image restoration and enhancement to improve on the SNR and CNR that preclude the current utility of digital

0091-3286/2010//$25.00 © 2010 SPIE



Downloaded from SPIE Digital Library on 02 Dec 2010 to 202.114.65.9. Terms of Use: http://spiedl.org/terms

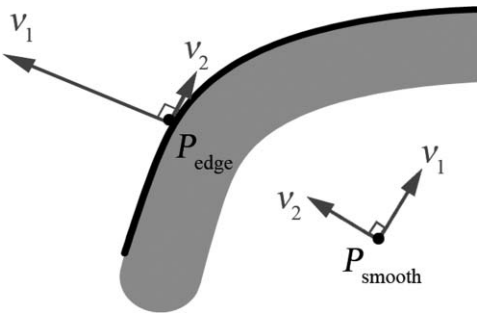


**Fig. 1** Eigenvectors at an edge pixel $P_{edge}$ and a smooth pixel $P_{smooth}$.

images for industry.[46] In the TFAB algorithm, it is possible to modulate all aspects of the diffusion behavior. Although the algorithm turns out to be effective for miscellaneous images, there are still several open problems. First, the spatial gradient makes it difficult to distinguish significant discontinuities from noise due to overlocalization, making the diffusion coefficient unreliable. Next, several parameters have to be tuned for a desirable diffusivity. If any proper parameters fail to be achieved, it is easy to lead to unsatisfactory results. Finally, edge orientations are not taken into account in the anisotropic diffusion discrete scheme, which is inefficient for edge-preserving smoothing. Apart from these efforts, we introduced a hyperspectral anisotropic diffusion scheme that takes into account the recent advances and the specificities of hyperspectral remote sensing.[45]

In this paper, we further develop our previous heuristic idea from an alternative perspective in order to come up with a region-based adaptive anisotropic diffusion (RAAD) algorithm. Unlike our earlier work, we first explore a region-segmentation approach to obtain a map contains different regions. Previously, Harris and Stephens[47] proposed a combined corner and edge detector for detecting feature points. In the Harris detector, the corner response function is used as a measure of corner and edge quality for region classification. Instead of the corner response function, we use the eigenvalue difference of the multiscale structure tensor of each pixel to classify an image into three regions representing the region's complexity. On the basis of the different types of regions, a variable weight is incorporated into the anisotropic diffusion partial differential equation (PDE) for compromising the FAB diffusion, so that our algorithm can adaptively encourage strong smoothing in homogeneous regions and suitable sharpening in detail and edge regions. Furthermore, we present an adaptive gradient threshold selection strategy. The threshold in a diffusion process determines to what extent edge features should be enhanced during smoothing. Selecting the threshold is a process of analyzing local contrast. Some papers have proposed automatic selection of the parameter.[17,28,48,49] We think that such an automatic strategy can be applied only to some specific applications, because the amount of desired smoothing is a user's choice. In this paper, the optimal gradient threshold is estimated as the mean of local intensity differences on the homogeneous regions. Also, we modify the anisotropic diffusion discrete scheme by taking into account edge orientations. Filter action should be stronger along the edge and weaker across the edge. Instead of the same weight in the directions of four nearest neighbors, we assign different weights in the directions of the eight nearest neighbors according to oriented patterns. As a result, important features are better enhanced, simultaneously, with noise removal. To sum up, we believe the RAAD algorithm to be a novel mechanism for image enhancement and denoising.

The remainder of this paper is organized as follows: Section 2 gives an overview of the state of the art in anisotropic diffusion filtering; Section 3 presents the proposed RAAD algorithm; Section 4 describes simulations including comparative results between several existing anisotropic diffusion schemes and our proposed algorithm; and Section 6 states our concluding remarks.

## 2 Recent Work on Anisotropic Diffusion

Perona and Malik[17] formulated an anisotropic diffusion filter as a process that encourages intraregional smoothing, while inhibiting interregional denoising. The Perona–Malik (P-M) nonlinear diffusion equation is of the following form:

$$\frac{\partial I(x,y,t)}{\partial t} = \mathrm{div}\{c\,[\nabla I(x,y,t)]\,\nabla I(x,y,t)\}, \tag{1}$$

where $\nabla$ is the gradient operator, div is the divergence operator, and $c(\cdot)$ is the diffusion coefficient, which is a nonnegative monotonically decreasing function of local spatial gradient. If $c(\cdot)$ is constant, then isotropic diffusion is enacted. In this case, all locations in the image, including the edges, are equally smoothed. This is an undesirable effect because the process cannot maintain the natural boundaries of objects. In terms of the anisotropic diffusion, the image denoising is defined as follows:[17]

$$I(x,y,t+1) = I(x,y,t) + \mathrm{div}[c(\nabla I)\nabla I]. \tag{2}$$

Perona and Malik[17] discretized their anisotropic diffusion equation as follows:

$$I\,(x,y,t+1) = I(x,y,t) + \frac{\lambda}{|\eta(x,y)|} \times \sum_{(p,q)\in\eta(x,y)} c\left[\nabla I_{(p,q)}^{(x,y)}\right]\nabla I_{(p,q)}^{(x,y)}, \tag{3}$$

where $I(x, y, t)$ is a discretely sampled image, $(x, y)$ denotes a pixel to be smoothed in the 2-D image domain, and $t$ denotes the discrete time steps (iterations). The constant $\lambda$ is a scalar that determines the rate of diffusion, $\eta(x, y)$ represents the spatial neighborhood of the pixel $(x, y)$, and $|\eta(x, y)|$ is the spatial the number of neighbors of pixel $(x, y)$. $\nabla I_{(y,q)}^{(x,y)}$ indicates the image intensity difference between two pixels at $(x, y)$ and $(p, q)$ to approximate the image gradient. For the four nearest neighbors of the pixel, the gradients in four directions can be calculated in the following way:

$$\begin{aligned}
\nabla I_{\mathrm{N}}(x,y) &= I(x,y-1,t) - I\,(x,y,t)\,,\\
\nabla I_{\mathrm{S}}(x,y) &= I(x,y+1,t) - I\,(x,y,t)\,,\\
\nabla I_{\mathrm{E}}(x,y) &= I(x+1,y,t) - I\,(x,y,t)\,,\\
\nabla I_{\mathrm{N}}(x,y) &= I(x-1,y,t) - I\,(x,y,t)\,.
\end{aligned} \tag{4}$$

The choice of the diffusion coefficient plays a significant role in edge preserving. Generally, as proposed in



Downloaded from SPIE Digital Library on 02 Dec 2010 to 202.114.65.9. Terms of Use: http://spiedl.org/terms

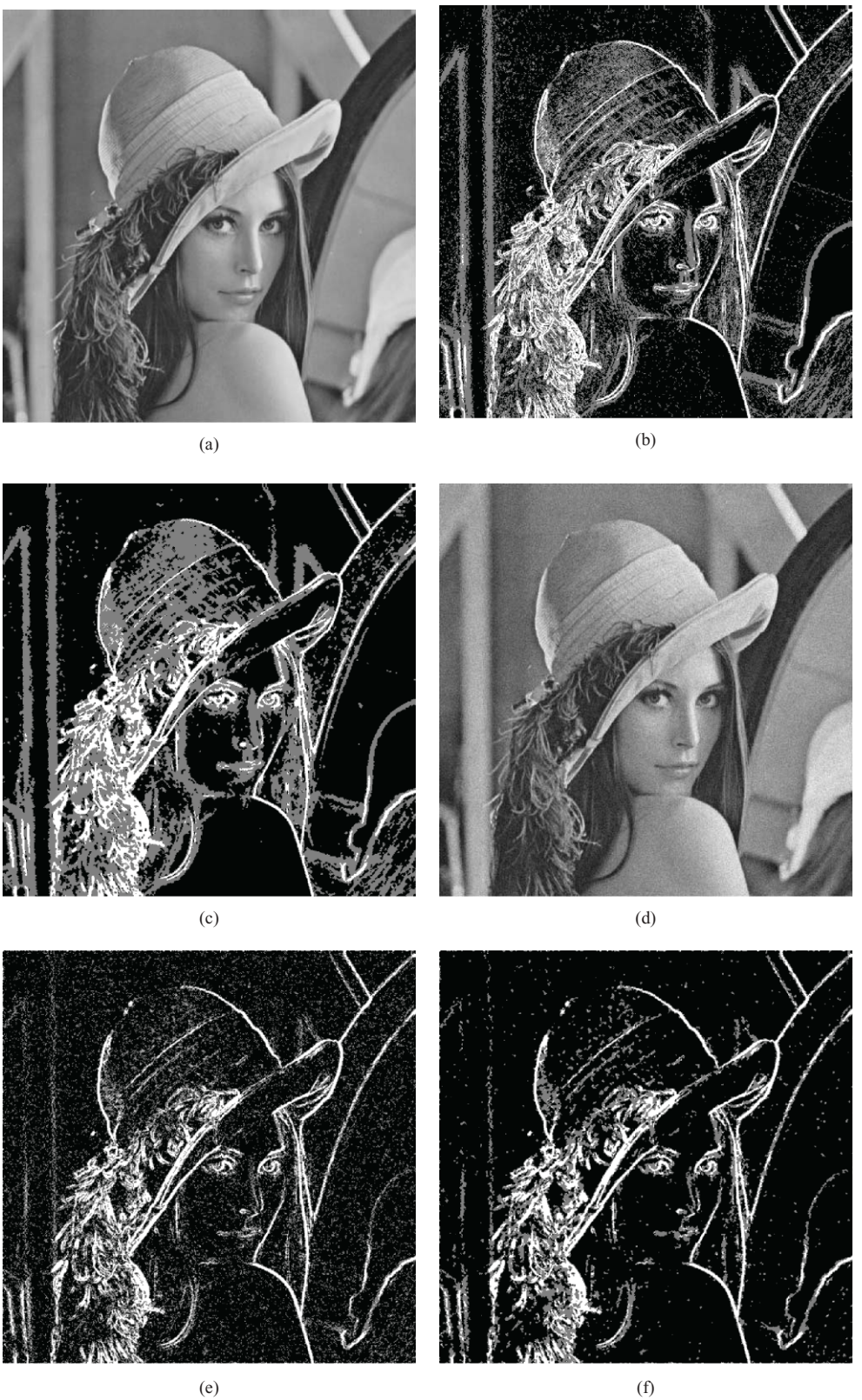

**Fig. 2** Region map for Lena image: (a) Original Lena image, (b) region map corresponding to (a) ($\sigma = 0.05$, $\rho = 0.1$), (c) region map corresponding to (a) processed by majority filtering ($\sigma = 0.05$, $\rho = 0.1$), (d) noisy lena image, (e) region map corresponding to (d) ($\sigma = 0.3$, $\rho = 0.8$), and (f) region map corresponding to (d) processed by majority filtering ($\sigma = 0.3$, $\rho = 0.8$).



Downloaded from SPIE Digital Library on 02 Dec 2010 to 202.114.65.9. Terms of Use: http://spiedl.org/terms

Perona–Malik's work,[17] it takes

$$c(\nabla I(x,y,t)) = \frac{1}{1+(\|\nabla I(x,y,t)\|/k)^{1+\alpha}}, \quad \text{where} \quad \alpha > 0$$

or

$$c[\nabla I(x,y,t)] = \exp\{-k[\|\nabla I(x,y,t)\|]^2\}, \tag{5}$$

where $\|\nabla I\|$ is the gradient magnitude and parameter $k$ serves as a gradient threshold: a smaller gradient is diffused, positions of a larger gradient are treated as edges. However, the P-M equation has several serious practical and theoretical difficulties. As Alvarez et al.[19] mentioned, the continuous P–M equation is ill posed with the diffusion coefficients in Eq. (5); very similar images can produce divergent solutions and therefore very different edges. This is caused by the fact that the diffusion coefficient $c$ used in[17] leads to flux decreasing for some gradient magnitudes and the scheme may work locally as the inverse diffusion that is known to be ill posed, and can develop singularities of any order in arbitrarily small time. As a result, a large gradient magnitude no longer surely represents true edges and the diffusion coefficients are not reliable, resulting in the unsatisfactory denoising performance.

So far, much research has been devoted to improving the Perona-Malik's anisotropic diffusion method. For example, Catte et al.[18] showed that the P-M equation can be made well posed by smoothing isotropically the image with a scaling parameter $\sigma$, before computing the image gradient used by the diffusion coefficient:

$$\frac{\partial I(x,y,t)}{\partial t} = \operatorname{div}\{c[\nabla I_\sigma(x,y,t)]\nabla I(x,y,t)\}. \tag{6}$$

Equation (6) corresponds to the regularized version of the P-M PDE, and $I_\sigma = G_\sigma(I) * I$ is a smoothed version of $I$ obtained by convolving the image with a zero-mean Gaussian kernel $G_\sigma$ of variance $\sigma^2$. Similarly, Torkamani–Azar et al.[50] replaced the Gaussian filter with a symmetric exponential filter and the diffusion coefficient is calculated from the convolved image. Although these improvements can convert the ill-posed problem[51] in the Perona–Malik's anisotropic diffusion method into a well-posed one, their reported enhancement and denoising performance can be further improved. Weickert proposed later a nonlinear diffusion coefficient that produces segmentation-like results[52] given by:

$$c(x,y,t) = \begin{cases} 1, & |\nabla I_\sigma(x,y,t)| = 0 \\ 1-\exp\left(-\frac{C_m}{(\|\nabla I(x,y,t)\|/k)^{2m}}\right), & |\nabla I_\sigma(x,y,t)| > 0 \end{cases} \tag{7}$$

where segmentation-like results are obtained using $m = 4$ and $C_4 = 3.31488$.

Meanwhile, anisotropic diffusion can be considered as a robust estimation procedure that estimates a piecewise smooth image from a noisy version. A different monotonically decreasing function is chosen to determine the anisotropic diffusion coefficient through robust statistics. Compared to the P-M method,[17] the robust anisotropic diffusion demonstrates improved automatic stopping of the diffusion process with preservation of sharp boundaries and better continuity of edges.[28] Black et al. proposed a more robust "edge-stopping" function derived from Tukey's biweight[28]

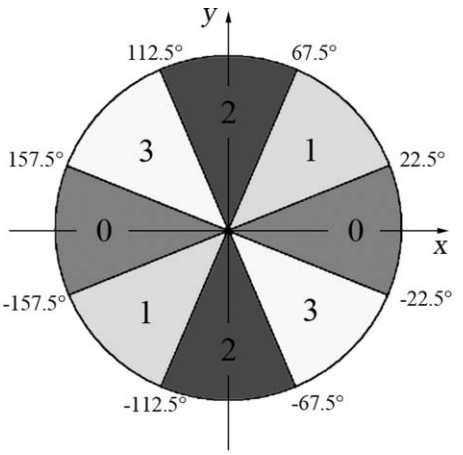


**Fig. 3** Relating edge direction to direction in an image.

$$c(x,y,t) = \begin{cases} \frac{1}{2}[1-(|\nabla I(x,y,t)|/\sigma_e)^2]^2 & |\nabla I(x,y,t)| \le \sigma_e, \\ 0, & \text{otherwise.} \end{cases} \tag{8}$$

where $\sigma_e$ is a robust scale threshold about the gradient magnitude. The robust anisotropic diffusion method can preserve sharper boundaries than previous schemes and improve the automatic stopping of the diffusion evolution. However, the method cannot minimize the effect of large oscillations of the gradient. Not long after this, a better behaved diffusion coefficient based on sigmoid function was proposed[32]

$$c(x,y,t) = 0.5 \cdot (1-\tanh\{\gamma \cdot [\|\nabla I(x,y,t)\| - k]\}), \tag{9}$$

where $\gamma$ controls the steepness of the min-max transition region of anisotropic diffusion and $k$ controls the extent of the diffusion region in terms of gradient gray level.

Note that all of anisotropic diffusion filters that we have investigated thus far utilize a scalar-valued diffusion coefficient $c$ that is adapted to the underlying image structure, Weickert[25,29,53] defined this "pseudoanisotropy" as "isotropic nonlinear," and pointed out that the consequence of isotropic nonlinear diffusion is that only the magnitude, not the direction of the diffusion flux, can be controlled at each image location. The noise close to edge features remains unfiltered due to the small flux in the vicinity of edges. To enable smoothing parallel to edges, Weickert proposed edge-enhancing diffusion by constructing the diffusion tensor based on an orientation estimate obtained from observing the image at a larger scale[29]

$$\frac{\partial I(x,y,t)}{\partial t} = \operatorname{div}\{\mathbf{D}[\nabla I_\sigma(x,y,t)] \cdot \nabla I(x,y,t)\}, \tag{10}$$

where $\mathbf{D}$ is a $2\times2$ diffusion tensor and is specially designed from the spectral elements of the structure tensor in order to anisotropically smooth the image, while taking into account its intrinsic local geometry, preserving its global discontinuities.



Downloaded from SPIE Digital Library on 02 Dec 2010 to 202.114.65.9. Terms of Use: http://spiedl.org/terms

(a) (b)

**Fig. 4** Regional enlarged portion of the original and noisy image of Lena: (a) Standard image and (b) noisy image of Lena with a noise variance of 225.

On the other hand, we review the developments of anisotropic diffusion from another direction. Instead of restricting the "minimum-maximum" principle, obeyed by most anisotropic diffusion processes, Gilboa et al.[37] proposed a diffusion coefficient that administrates the Gilboa–Sochen–Zeevi (GSZ) FAB diffusion process, where a negative diffusion coefficient is incorporated into image-sharpening and enhancement processes to deblur and enhance the extremes of the initial signal

$$c\left[\nabla I\left(x,y,t\right)\right]=\frac{1}{1+\left[\left\|\nabla I\left(x,y,t\right)\right\|/k_{\mathrm{f}}\right]^{n}}-\frac{\alpha}{1+\left\{\left[\left\|\nabla I\left(x,y,t\right)\right\|-k_{\mathrm{b}}\right]/w\right\}^{2m}}, \quad (11)$$

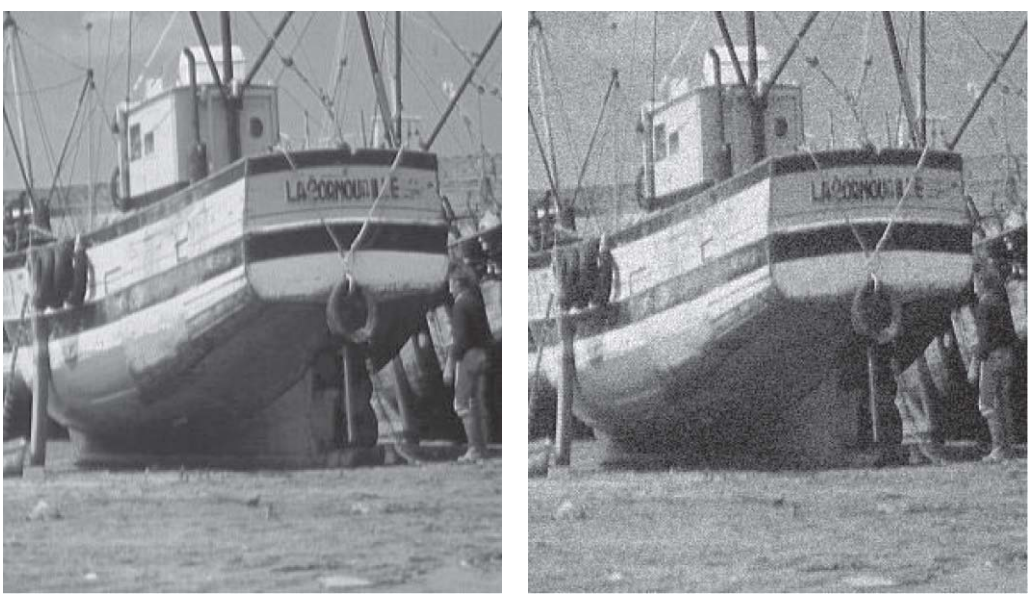

(a) (b)

**Fig. 5** Regional enlarged portion of the original and noisy image of Boat: (a) Standard image and (b) noisy image of Boat with a noise variance of 225.



Downloaded from SPIE Digital Library on 02 Dec 2010 to 202.114.65.9. Terms of Use: http://spiedl.org/terms

where $k_f$ is similar to the role of the $k$ parameter in the P-M diffusion equation; $k_b$ and $w$ define the range of backward diffusion and are determined by the value of the gradient that is emphasized; $\alpha$ controls the ratio between the FAB diffusion; and the exponent parameters $(n, m)$ are chosen as $(n = 4, m = 1)$. Equation (11) is locally adjusted according to image features, such as edges, textures, and moments. The Gilboa's FAB diffusion process can therefore enhance features while locally denoising the smoother segments of images.

However, the transition length between the maximum and minimum coefficient values varies with the gradient threshold, which makes controlling diffusion difficult.[43] Thus, we propose the LVCFB diffusion coefficient as follows:[43]

$$c[\nabla I(x,y,t)] = \frac{1-\tanh\{\beta_1\cdot[\|\nabla I(x,y,t)\|-k_f]\}-\alpha\cdot(1-\tanh^2\{\beta_2\cdot[k_b-\|\nabla I(x,y,t)\|]\})}{2}, \tag{12}$$

where $\beta_1$ and $\beta_2$ control the steepness for the min-max transition region of forward diffusion and backward diffusion, respectively. These two parameters are vital to the FAB diffusion behavior and the transition width from isotropic to oriented flux can be altered by modulating them. In addition, our diffusion process can preserve the transition length from isotropic to oriented flux, and thus, it is better at controlling the diffusion behavior than that of the Gilboa's FAB diffusion.

## 3 RAAD Algorithm

In this section, we propose a RAAD algorithm. We first demonstrate a region-based segmentation, and then present the RAAD algorithm and an adaptive estimation of the gradient threshold in the corresponding diffusion coefficient. Finally, we implement anisotropic diffusion discrete scheme taking into account edge orientations.

### 3.1 *Region-Based Adaptive Segmentation*

It is well documented that discontinuities in an image are likely to correspond to important features. However, noise corruption can generate discontinuities as well.[54] Therefore, how to measure discontinuities is very significant. As a common local measure in image processing, spatial gradient is used to detect variable local discontinuities and is sensitive to any local intensity change. Nevertheless, it is difficult for this measure to distinguish significant discontinuities from noise. One possibility how to describe the local image information is to employ the structure tensor.

Harris and Stephens[47] describes the Plessey feature point detector and points out that the variation of the autocorrelation over different orientations can be found by calculating functions related to the principle curvatures of the local autocorrection. However, location accuracy in noisy images is poor. Furthermore, the region-classification strategy of the Harris detector is mainly used for detecting corner points instead of improving the performance of anisotropic diffusion. Finally, the region-classification results are often accompanied by small-size segments and isolated points. In this paper, the eigenvalue difference of the structure tensor is served as a measure of the region's complexity. The complexity measure is not only easy to calculate but can also be theoretically justified. In addition, instead of the structure matrix, we use a multiscale structure tensor, which is obtained by a componentwise Gaussian convolution of the structure matrix, to reduce the noise effect on the eigenvalues. Lastly, a majority filter is performed to eliminate the undesirable segments. For the sake of clarity, the region-based adaptive segmentation is briefly described.

In order to identify gradients with the same orientation but of opposite directions, the gradient can be reconsidered in a matrix framework. A structure matrix $\boldsymbol{S}_0$ can be formed by a tensor product of the gradient vectors,

$$\boldsymbol{S}_0 = \begin{pmatrix} s_{11} & s_{12} \\ s_{21} & s_{22} \end{pmatrix} = \nabla I_\sigma \otimes \nabla I_\sigma = \nabla I_\sigma \nabla I_\sigma^T. \tag{13}$$

The matrix $\boldsymbol{S}_0$ processes an orthonormal basis of eigenvectors $\vec{v}_1, \vec{v}_2$ with $\vec{v}_1 \| \nabla I_\sigma$ and $\vec{v}_2 \perp \nabla I_\sigma$ (see Fig. 1). The information contained in the matrix $\boldsymbol{S}_0$ is already sufficient to control a combined diffusion (of different amounts) in the directions parallel and perpendicular to the gradient, so as to remove the small-scale noise both in homogeneous regions and at the edges without blurring the discontinuities in image intensity. However, the local information cannot provide enough clues if we were after coherence enhancement (e.g., the restoration of interrupted linelike structures as in Ref. 46). Also, noise always affects the eigenvalues. In such cases, information from some neighborhood has to be assembled. This can be attained by a componentwise convolution of the matrix $\boldsymbol{S}_0$ with a Gaussian $G_\rho$, where the integration scale $\rho(\rho \geq 0)$ should reflect the characteristic window size over which the orientation is to be analyzed. Thus, a 2-D structure tensor is introduced by

$$\boldsymbol{S}_\rho(\nabla I_\sigma) = G_\rho * (\nabla I_\sigma \otimes \nabla I_\sigma). \tag{14}$$

Weickert[29] named the matrix $\boldsymbol{S}_\rho$ structure tensor. The matrix is symmetric, positive semidefinite, possesses orthonormal eigenvectors $\vec{v}_1, \vec{v}_2$ with

$$\vec{v}_1 \| \left[2s_{12}, s_{11}-s_{22}+\sqrt{(s_{11}-s_{22})^2+4s_{12}^2}\right]^T, \quad \vec{v}_2 \perp \vec{v}_1 \tag{15}$$

and the corresponding eigenvalues $\lambda_+, \lambda_-$ are defined as follows:

$$\lambda_\pm = \frac{1}{2}\left[s_{11}+s_{22} \pm \sqrt{(s_{11}-s_{22})^2+4s_{12}^2}\right]. \tag{16}$$

The eigenvalues describe the average, integrated contrast in the eigendirections; because $\lambda_+ \geq \lambda_- \geq 0$, $\vec{v}_1$ is the orientation of the highest gray-value fluctuations, whereas $\vec{v}_2$ gives the prevailing local orientation, or coherence direction. Furthermore, the eigenvalues can be used to analyze the local



Downloaded from SPIE Digital Library on 02 Dec 2010 to 202.114.65.9. Terms of Use: http://spiedl.org/terms

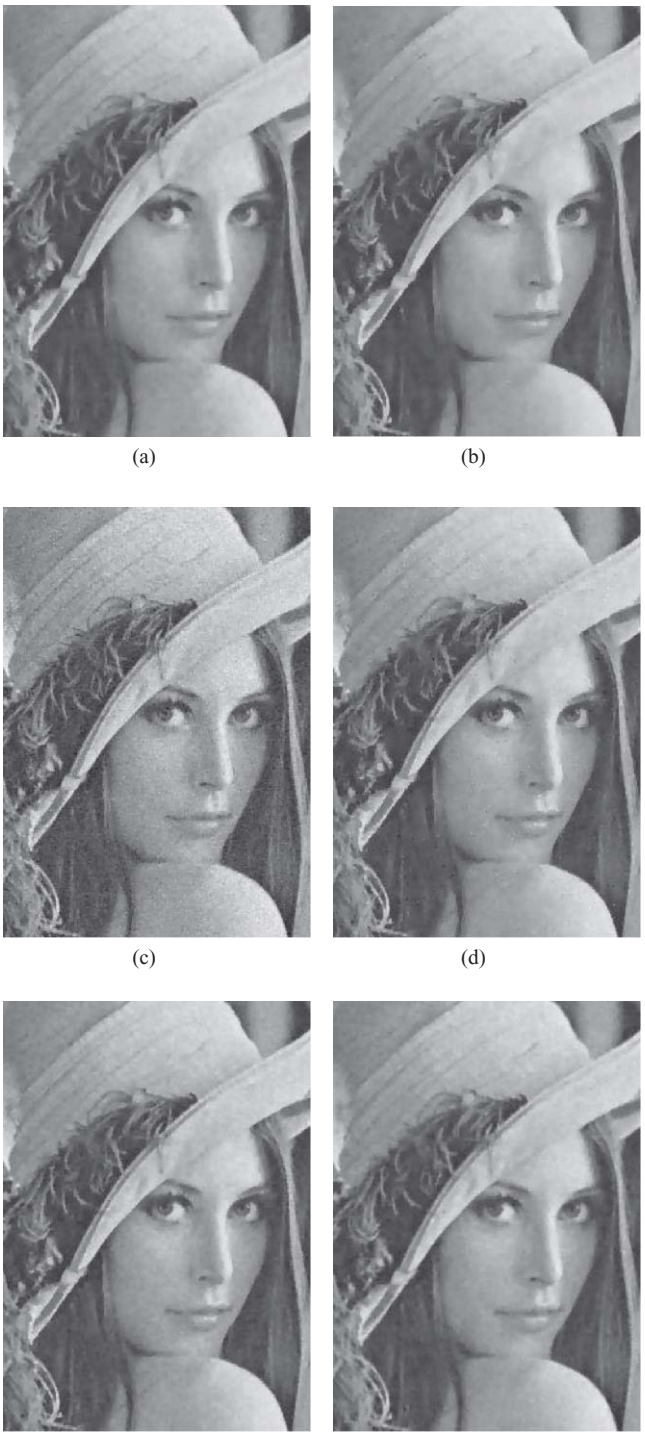

**Fig. 6** Enhanced images for Lena image: (a) Enhanced Lena with CAD, (b) WAD, (c) RAD, (d) MAD ($\gamma = 0.1$), (e) EED, and (f) RAAD ($\sigma = 0.5$, $\rho = 1$, $\delta_{\text{smooth}} = 0$, $\delta_{\text{detail}} = 0.2$, $\delta_{\text{edge}} = 0.3$) (10 iterations).

structure: $\lambda_+ = \lambda_- = 0$ in constant areas, straight edges lead to $\lambda_+ \gg \lambda_- = 0$, corners can be identified by $\lambda_+ \geq \lambda_- \gg 0$, and thus, the expression $|\lambda_+ - \lambda_-|$ may serve as a measure of the local variance of the pixel. These properties can be exploited to control the amount of diffusion in the specific direction.

For region segmentation using eigenvalues of the structure tensor, we propose the following strategy:

$$I(x, y) \in \begin{cases} \text{homogeneous region} & \text{if } |\lambda_+ - \lambda_-| \leq T_{\text{smooth}} \\ \text{edge region} & \text{if } |\lambda_+ - \lambda_-| \geq T_{\text{edge}} \\ \text{detail region} & \text{otherwise,} \end{cases} \tag{17}$$

where $I(x, y)$ denotes the region type of pixel $(x, y)$. For robust region segmentation, the proper modulation of the threshold values $T_{\text{smooth}}$ and $T_{\text{edge}}$ is required. Note from the above discussion that $|\lambda_+ - \lambda_-|$ is closely related to the local variance of the pixel, we can set the threshold values as[55]

$$\begin{aligned} T_{\text{smooth}} &= t^2_{\text{smooth}} + \hat{\sigma}^2_n, \\ T_{\text{edge}} &= \beta \sigma^2_{\text{edge}}, \end{aligned} \tag{18}$$

where $\sigma^2_n$ denotes the estimated noise variance of $I$ and $t_{\text{smooth}}$ is a tolerant parameter of intensity variation in a smooth region. Meanwhile, the optimal value of the edge variance $\sigma^2_{\text{edge}}$ is always around the mean of local variances of the pixels having a local variance larger than $T_{\text{smooth}}$. $\beta$ is a constant controlling the ratio between detail and edge regions.

The region-classification map generated using Eq. (17) may result in undesired small-size segments due to the pixelwise segmentation and noise. One way to eliminate these segments is using a particular type of spatial filter called a majority filter. In this case, as the kernel passes over the image, the central pixel is set to the majority value within the kernel. This means that if there is a dark pixel surrounded by mostly white pixels, the output pixel will be set to white. This tends to remove small regions surrounded by much larger areas of a fixed value. As a demonstration, the region maps for Lena image and its noisy version ($\sigma^2 = 100$) are illustrated in Figs. 2(b), 2(c), 2(e), and 2(f), respectively. In the region map, black regions are homogeneous, gray regions represent detail regions, and white regions manifest the inhomogeneities that indicate most of the important features (e.g., the girl's eyes and the hat decoration). It is evident that the region map in Fig. 2 readily indicates locations of highly homogeneous, detail, and edge regions.

### 3.2 *RAAD*

In this section, we present a RAAD algorithm based on FAB diffusion. In Eqs. (11) and (12), $\alpha$ is the weight for balancing the forward and backward diffusion. However, it is fixed as a constant for all pixels in the image, which is not sufficient for edge-enhancing smoothing in noise circumstance. We believe that this parameter should be modulated with respect to different regions: a very small value for homogeneous regions to guarantee the dominance of the forward diffusion, and a relative large value for edge and detail regions to enhance edge features and fine detail. Thus, we present a novel region-based diffusion coefficient, as follows:

$$c[\nabla I(x, y, t)] = \frac{1}{\sqrt{1 + [\|\nabla I(x, y, t)\|/k_{\text{f}}]^2}} - \frac{\alpha(x, y)}{1 + [\|\nabla I(x, y, t)\|/k_{\text{b}}]^2} \tag{19}$$



Downloaded from SPIE Digital Library on 02 Dec 2010 to 202.114.65.9. Terms of Use: http://spiedl.org/terms

with

$$\alpha(x, y) = \begin{cases} \delta_{\text{smooth}} & I(x, y) \in \text{homogeneous regions} \\ \delta_{\text{edge}} & I(x, y) \in \text{edge regions} \\ \delta_{\text{detail}} & I(x, y) \in \text{detail regions}, \end{cases} \tag{20}$$

where $\delta_{\text{smooth}}$, $\delta_{\text{edge}}$, and $\delta_{\text{detail}}$ are the variable region-based weights and selected within the bound: $\delta_{\text{smooth}} > \delta_{\text{edge}} > \delta_{\text{smooth}} \geq 0$. $k_{\text{f}}$ and $k_{\text{b}}$ are the gradient thresholds of the proposed diffusion coefficient, and we will return to modulating them later on.

In an anisotropic diffusion network, the decision of the gradient threshold that classifies an image into homogenous and edge regions is very important. If the user wants to obtain a coarse-scale image with only the key edges, a large $k$ should be specified, while if a fine-scale image with all the detailed edges is required, a small $k$ should be chosen. To appropriately separate edges from noise, the optimal value of $k$ should be around the mean of local intensity differences in homogeneous regions. However, it is still necessary to discover whether a pixel is in an edge feature region or a homogeneous region in all the above strategies for estimating $k$.

Indeed, because the noise is assumed to be randomly distributed in the image space, a practical way of estimating its variance is to consider homogeneous regions, where small variations or texture are mainly due to noise. Thus, in order to estimate the gradient threshold, we use the mean of local intensity differences on the homogeneity map. However, in contrast to previous work, only homogeneous regions generated by the region-based adaptive segmentation mentioned in Section 3.1 are taken into account in this estimation. This analysis is performed at each iteration, and a new threshold $k$ value is automatically determined. As time advances, only smoother and smoother regions are being filtered. Therefore, the gradient threshold can adaptively decrease with $t$. For the proposed algorithm, our simulations on various images, including those not reported here, uncover that the optimal values of two gradient thresholds in Eq. (19) are modulated by $\lfloor k_{\text{f}}, k_{\text{b}} \rfloor = [1, 2] * k$.

### 3.3 *Edge-Orientation–Driven Discretization Scheme*

The filter behavior has to adapt to the regions of the image where it is applied. Three different kinds of regions are considered in this paper. The first are homogeneous regions, where the filter action should be a maximum; because no details are present, each intensity variation or texture can be regarded as noise. The second are detail regions, where the filter action should be very slight to preserve the fine details. The edge features zones should also be taken into account, where the filter action should be a slighter even inverse diffusion to enhance edges. Although all three regions are considered in Perona and Malik's anisotropic diffusion scheme (3), not enough care is taken for edges. Actually, no attention is given to the edge directions, as a result they are always considered to be displaced vertically or horizontally.[56] Moreover, one cannot recognize whether a slight intensity variation is mainly due to a slow varying edge or to noise; thus, it is unreasonable that both situations are treated in the same way. In this paper, our work focuses on the computation of the diffusion coefficients by taking into account the gradient intensities across edges when the pixel $I(x, y)$ resides in edge regions. Specifically, filter action should be stronger in the direction along the edge, and weaker in the perpendicular direction. Meanwhile, new terms can be inserted in the discretization of the diffusion equation for handling edge directions. In order to accomplish the assumptions mentioned above, we propose the following anisotropic diffusion equation:

$$\begin{aligned} I(x, y, t+1) = I(x, y, t) \\ &+ \lambda[W_{\text{V}}(\theta) \cdot (c_{\text{N}} \cdot \nabla_{\text{N}} I + c_{\text{S}} \cdot \nabla_{\text{S}} I) \\ &+ W_{\text{H}}(\theta)(c_{\text{E}} \cdot \nabla_{\text{E}} I + c_{\text{W}} \cdot \nabla_{\text{W}} I)] \\ &+ \lambda[W_{\text{D}_1}(\theta) \cdot (c_{\text{NE}} \cdot \nabla_{\text{NE}} I + c_{\text{SW}} \cdot \nabla_{\text{SW}} I) \\ &+ W_{\text{D}_2}(\theta)(c_{\text{NW}} \cdot \nabla_{\text{NW}} I + c_{\text{SE}} \cdot \nabla_{\text{SE}} I)], \end{aligned} \tag{21}$$

where $N$, $S$, $E$, $W$, NE, SW, NW, and SE are the mnemonic subscripts for eight directions (i.e., North, South, East, West, Northeast, Southwest, Northwest, and Southeast). The symbol $\nabla$ stands for nearest-neighbor differences. $\lambda$ is the time step: $0 \leq \lambda \leq 1/8$ for the numerical scheme to be stable. $\theta$ is the edge direction at pixel $(x, y)$, $W_{\text{v}}(\theta)$, $W_{\text{H}}(\theta)$, $W_{\text{D}_1}(\theta)$, and $W_{\text{D}_2}(\theta)$ are weights for different edge directions.

In order to find the edge direction at pixel $(x, y)$, the four neighborhoods are not sufficient; thus, a larger region is necessary to estimate what its orientation is. The problem of estimating the main orientation of a pixel pattern can be considered as the problem to find the direction, in each point of the considered neighborhood, the maximum numbers of orientations of the variation of the gradient magnitude. In this paper, the image is subdivided into nonoverlapping blocks of the same size, typically between $8 \times 8$ and $32 \times 32$ pixels. The gradient-based edge-orientation histogram is then calculated in each block. If we let $N$ be the total number of observations and $n$ be the total number of bins, the histogram $H_i$ meets the following conditions:

$$N = \sum_{i=1}^{n} H_i(x, y). \tag{22}$$

In the histogram, 360 deg is grouped in 20 groups, each of which is 18 deg, and we obtain $n = 20$. Thus, the main orientation in each block is defined as follows:

$$\theta = \vartheta + \frac{\pi}{2} = \arctan\left(\text{index}\frac{\pi}{10}\right) + \frac{\pi}{2} \tag{23}$$

and

$$\text{index} = \arg\max\{i | H_i(x, y)\} \quad (i = 1, 2, \ldots, 20), \tag{24}$$

where $\vartheta$ is the main gradient direction by calculating the histogram of the gradient direction for each pixel $(x, y)$ in the block and arctan is the inverse tangent function. We assume that, if an intensity variation between two zones is present, then the edge has to be located along the perpendicular direction. The calculation of orientation histogram can be performed in real time. Furthermore, the comparison of orientation histograms can be performed using a Euclidian distance that is very fast to compute for vectors whose dimensions are 20.

After the estimation of the edge direction has been performed, the functions $W_{\text{v}}(\theta)$, $W_{\text{H}}(\theta)$, $W_{\text{D}_1}(\theta)$, and $W_{\text{D}_2}(\theta)$ must be defined. These functions can be arbitrarily chosen. The only constraint to be satisfied with the aim of maintaining



Downloaded from SPIE Digital Library on 02 Dec 2010 to 202.114.65.9. Terms of Use: http://spiedl.org/terms

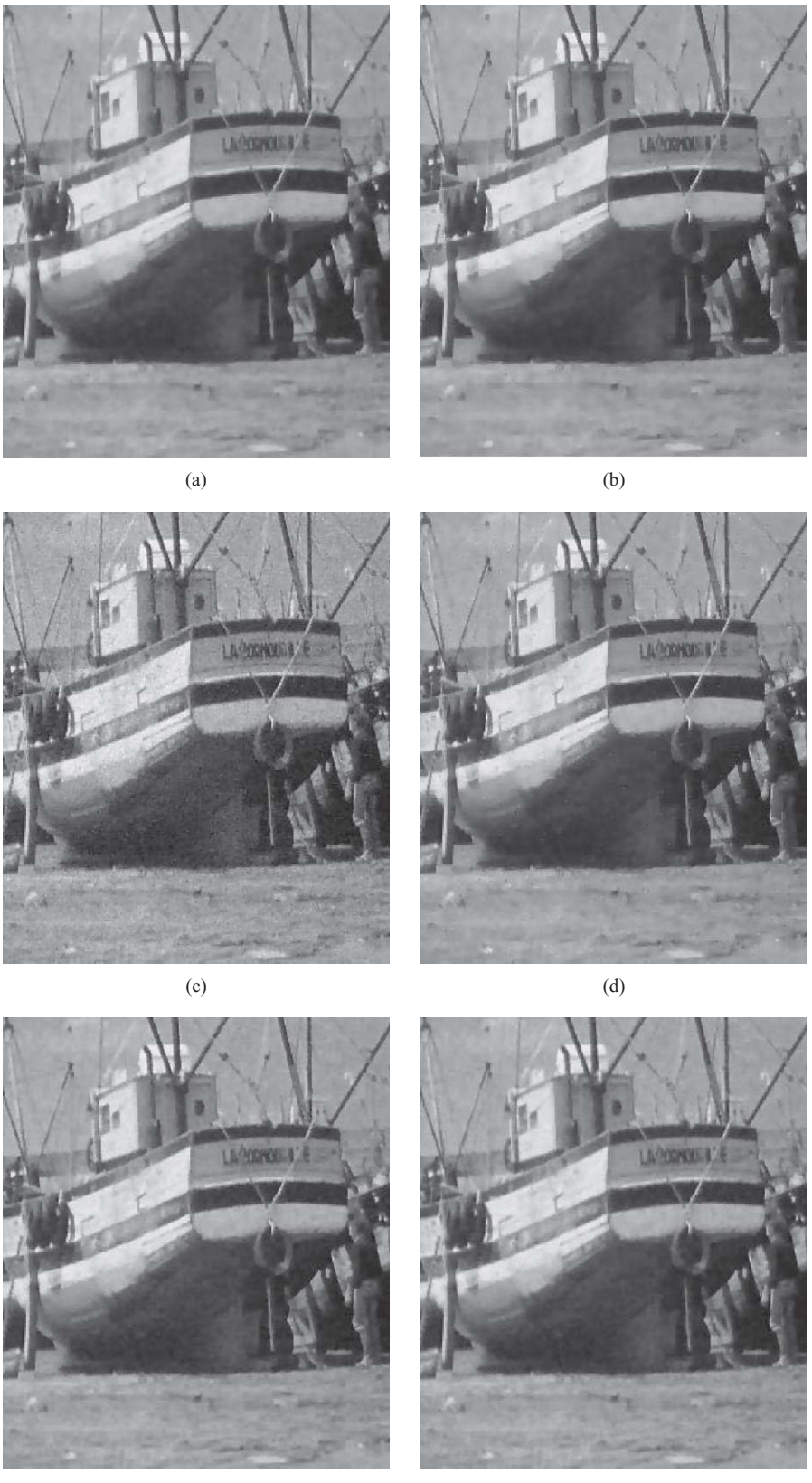

(a) (b) (c) (d) (e) (f)

**Fig. 7** Enhanced images for Boat image: (a) Enhanced Boat with CAD, (b) WAD, (c) RAD, (d) MAD ($\gamma = 0.1$), (e) EED, and (f) RAAD ($\sigma = 0.5$, $\rho = 1$, $\delta_{\text{smooth}} = 0.1$, $\delta_{\text{detail}} = 0.2$, $\delta_{\text{edge}} = 0.3$) (10 iterations).



Downloaded from SPIE Digital Library on 02 Dec 2010 to 202.114.65.9. Terms of Use: http://spiedl.org/terms

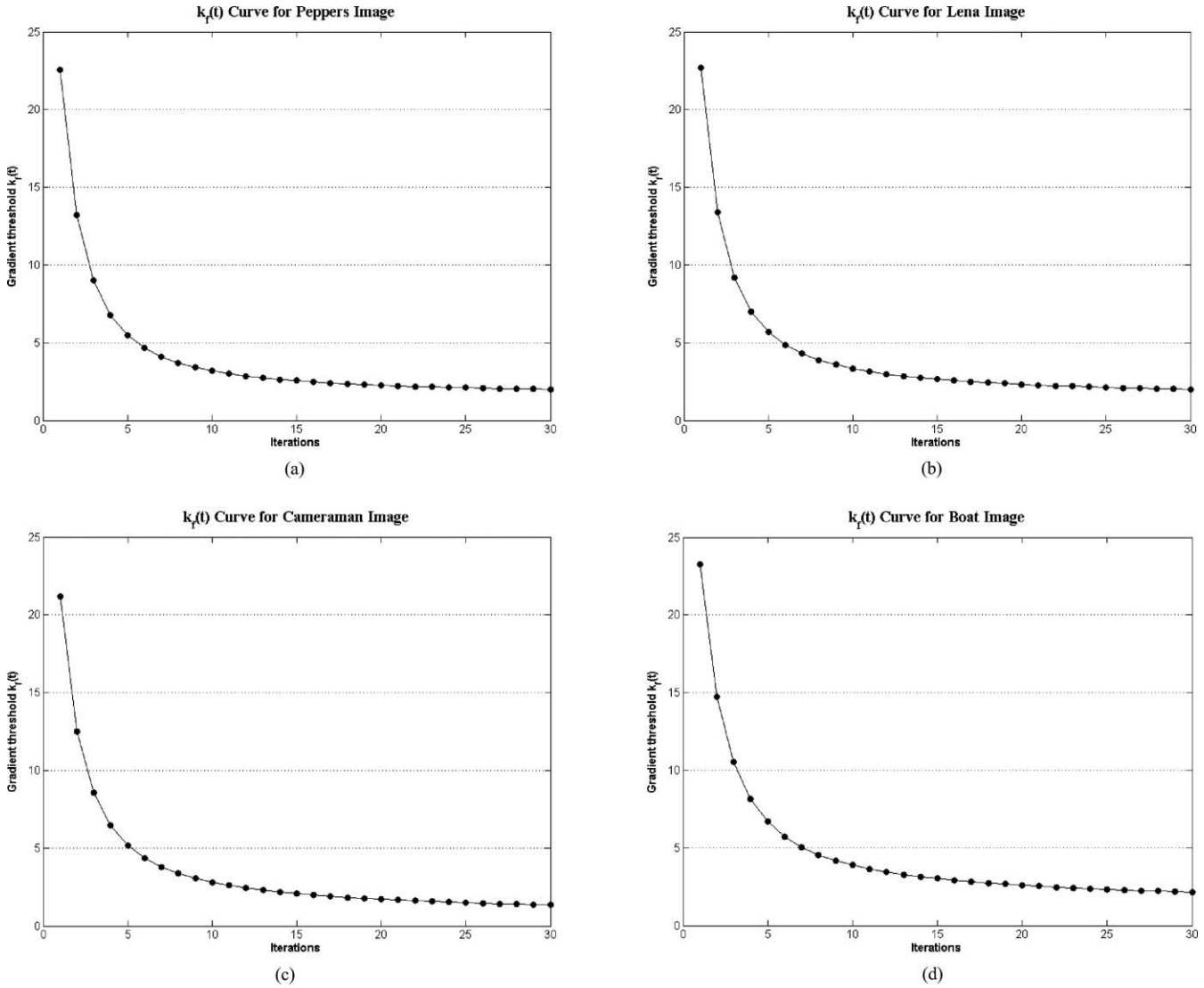


**Fig. 8** Gradient threshold evolution curves for the images of Peppers, Lena, Cameraman, and Boat with respect to noise variance 400.

the numerical stability of the process is

$$W_{\mathrm{V}}(\theta)\cdot(c_{\mathrm{N}}+c_{\mathrm{S}})+W_{\mathrm{H}}(\theta)\cdot(c_{\mathrm{E}}\cdot+c_{\mathrm{W}})+W_{\mathrm{D}_1}(\theta)\cdot(c_{\mathrm{NE}}+c_{\mathrm{SW}})+W_{\mathrm{D}_2}(\theta)\cdot(c_{\mathrm{NW}}+c_{\mathrm{SE}})\leq\frac{1}{\lambda}. \tag{25}$$

In order to illustrate our presentation, we divide the $x-y$ coordinate plane into eight quadrants by the four axes. These quadrants are identified by the Arabian numerals 0–3 in Fig. 3, where we define five domains as follows:

$$\Omega=\begin{cases}\Omega_0 & -\pi/8\leq\theta\leq\pi/8 \quad \text{or} \quad 7\pi/8\leq\theta\leq\pi \quad \text{or} \quad -\pi\leq\theta\leq-7\pi/8\\ \Omega_1 & \pi/8\leq\theta\leq3\pi/8 \quad \text{or} \quad -7\pi/8\leq\theta\leq-5\pi/8\\ \Omega_2 & 3\pi/8\leq\theta\leq5\pi/8 \quad \text{or} \quad -5\pi/8\leq\theta\leq-3\pi/8\\ \Omega_3 & 5\pi/8\leq\theta\leq7\pi/8 \quad \text{or} \quad -3\pi/8\leq\theta\leq-\pi/8.\end{cases} \tag{26}$$

Taking into account the previous equation and the fundamental trigonometric relation, the most suitable choice in this paper for $W_{\mathrm{V}}(\theta)$, $W_{\mathrm{H}}(\theta)$, $W_{\mathrm{D}_1}(\theta)$, and $W_{\mathrm{D}_2}(\theta)$ is

$$W_{\mathrm{V}}(\theta)=\begin{cases}0 & \theta\in\Omega_1 \quad \text{or} \quad \theta\in\Omega_3\\ \cos^2\theta & \theta\in\Omega_0\\ \sin^2\theta & \theta\in\Omega_2,\end{cases} \tag{27}$$



Downloaded from SPIE Digital Library on 02 Dec 2010 to 202.114.65.9. Terms of Use: http://spiedl.org/terms

(a) (b) (c)

**Fig. 9** Enhanced images for Lena image: (a) Enhanced Lena with GSZ FAB diffusion, (b) LVCFAB diffusion, and (c) RAAD ($\sigma = 0.5$, $\rho = 1$, $\delta_{\text{smooth}} = 0$, $\delta_{\text{detail}} = 0.2$, $\delta_{\text{edge}} = 0.3$) (10 iterations).

$$W_{\text{H}}(\theta) = \begin{cases} 0 & \theta \in \Omega_1 \quad \text{or} \quad \theta \in \Omega_3 \\ 1 - W_{\text{V}}(\theta) & \text{otherwise,} \end{cases} \tag{28}$$

$$W_{\text{D}_1}(\theta) = \begin{cases} \cos^2(\theta - \pi/4) & \theta \in \Omega_1 \\ \sin^2(\theta + \pi/4) & \theta \in \Omega_3 \\ 0 & \text{otherwise,} \end{cases} \tag{29}$$

$$W_{\text{D}_2}(\theta) = \begin{cases} 0 & \theta \in \Omega_2 \\ 1 - W_{\text{D}_1}(\theta) & \text{otherwise.} \end{cases} \tag{30}$$

It is obvious that we can demonstrate the different forms of the discretization equation by taking into account oriented patterns. For instance, if $\theta \in \Omega_0$, then substituting these functions in the modified anisotropic diffusion equation (18) leads to the following:

$$\begin{aligned} I(x, y, t+1) = I(x, y, t) \\ + \lambda[\cos^2\theta \cdot (c_{\text{N}} \cdot \nabla_{\text{N}} I + c_{\text{S}} \cdot \nabla_{\text{S}} I) \\ + \sin^2\theta (c_{\text{E}} \cdot \nabla_{\text{E}} I + c_{\text{W}} \cdot \nabla_{\text{W}} I)]. \end{aligned} \tag{31}$$

In this case, it is easy to infer that the edge orientation should approximate to the vertical direction according to the fact that the edge direction is always perpendicular to the gradient direction. During the diffusion process, a relatively large-weight $\cos^2\theta$ is assigned in the vertical direction to guarantee that the diffusion should mainly occur in the direction parallel to the edge, while a relatively small-weight $\sin^2\theta$ is assigned in the horizontal direction to ultimately avoid diffusion across the edge.

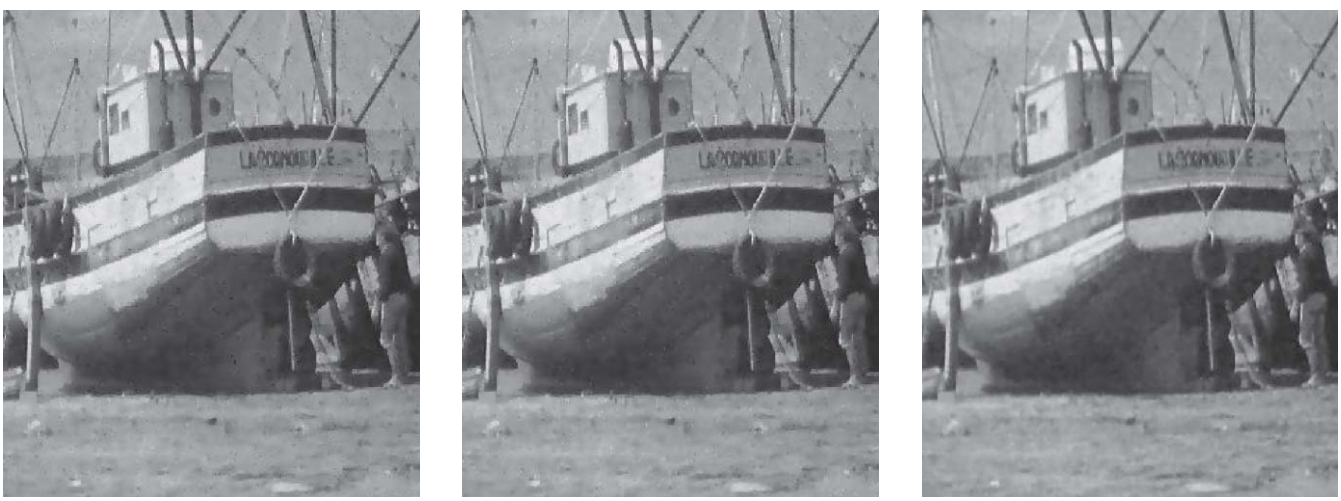

(a) (b) (c)

**Fig. 10** Enhanced images for boat image: (a) Enhanced boat with GSZ FAB diffusion, (b) LVCFAB diffusion, and (c) RAAD ($\sigma = 0.5$, $\rho = 1$, $\delta_{\text{smooth}} = 0.1$, $\delta_{\text{detail}} = 0.2$, $\delta_{\text{edge}} = 0.3$) (10 iterations).



Downloaded from SPIE Digital Library on 02 Dec 2010 to 202.114.65.9. Terms of Use: http://spiedl.org/terms

### 3.4 *RAAD Algorithm*

In this section, we summarize the ideas of the region-based adaptive segmentation and edge orientation-driven discretization scheme into a complete and adaptive image restoration and enhancement algorithm. To achieve this goal, we propose to filter the data by the following RAAD scheme.

**Algorithm 1. Region-Based Adaptive Anisotropic Diffusion**

1. Initialize the image data $I.I$ $(x, y, 0)$ denotes the original intensity of pixel $(x, y)$.
2. Initialize the diffusion parameters. Set parameters of the noise scale $\sigma$, the integration scale $\rho$, the maximum number of iterations $T$, the region-based weights $\delta_{\text{smooth}}$, $\delta_{\text{edge}}$, and $\delta_{\text{detail}}$.
3. Examine the eigenvalue difference of each pixel and determine its region type.
4. Iterate the diffusion filtering until $t = T$.
   a. The gradient thresholds $k_{\text{f}}$ and $k_{\text{b}}$ are estimated by the region map generated in step 3.
   b. For each pixel $(x, y)$, the diffusion coefficient $c[\nabla I(x, y, t)]$ is computed by Eq. (19). In homogeneous and detail regions, the traditional four nearest-neighbor diffusion discretization equation is perform to update $I$ $(x, y, t)$; while in edge regions, the eight nearest-neighbor diffusion discretization equation Eq. (21) is performed to update $I$ $(x, y, t)$. Our FAB diffusion algorithm is a discretization on a $3 \times 3$ lattice.

The step 3 of Algorithm 1 consists of following steps (assuming the current data in $I$; see Section 3.1 for details on the procedure).

**Algorithm 2. Region Segmentation**

1. Calculate the structure tensor $\boldsymbol{S}_p$
   a. Obtain the regularized image $s = I_\sigma$.
   b. Compute the gradient of the smoothed image, $\nabla s = (d_x, d_y)^T$ (using finite differences).
   c. Form the zero-order structure tensor, $\boldsymbol{S}_0 = \begin{pmatrix} d_x^2 & d_x \cdot d_y \\ d_x \cdot d_y & d_y^2 \end{pmatrix}$.
   d. If the integration scale $\rho$ is nonzero, calculate a componentwise convolution $\boldsymbol{S}_\rho(\nabla I_\sigma) = G_\rho * \boldsymbol{S}_0$.
2. Region segmentation
   a. Get eigenvalues $\lambda_+, \lambda_-$ of the matrix $\boldsymbol{S}_p$.
   b. Determine the region type of each pixel by comparing its eigenvalue difference $|\lambda_+ - \lambda_-|$ with the region-based weighted parameters $\delta_{\text{smooth}}$, $\delta_{\text{edge}}$, and $\delta_{\text{detail}}$.

## 4 Experiments

In this section, we first describe the methodology used in our simulations and then show comparative filtering results for a variety of blurred and noisy images. Finally, we demonstrate that as a useful tool for early vision, the proposed algorithm effectively enhances fine edge structures from medical images.

Chen classified the existing performance evaluation methods into three categories, i.e., subjective, objective, and application-based methodologies.[57] By the subjective methodology, a noisy image and its enhanced images are visually compared. Thus, the evaluation on the performance of an algorithm is dependent on human's common sense gained from a very sophisticated visual perception experience. By the objective methodology, an evaluation is performed by comparing the enhanced image and its original uncorrupted version to see how much noise has been removed from a noisy image. By the application-based methodology, images in a certain application field are used for tests and the enhancing results are assessed by a specialist who has expertise in the field or a comparison to an anticipated result set up prior to the test.

For demonstrating the effectiveness of the proposed algorithm in noise reduction and edge preservation, the RAAD is first compared to five counterparts of Catte's anisotropic diffusion by (CAD),[18] robust anisotropic diffusion (RAD),[28] Monteil's anisotropic diffusion (MAD),[32] Weickert's anisotropic diffusion (WAD)[52] and edge-enhancing diffusion (EED),[29] in detail from visual quality and quantitative analyses of the denoised images. The critical value $k$ should be chosen according to the noise level and edge strength. In our experiments, we set $k$ in different diffusion schemes by referring to the original papers. The ultimate goal of image enhancement is to facilitate the subsequent processing for early vision. To demonstrate the usefulness of our algorithm in an early vision task, we apply our algorithm to performing edge-enhancing filtering on medical images for an application-based evaluation.

In order to objectively evaluate the performance of the different diffusion algorithms, we adopt two noise-reduction measures: peak SNR (PSNR) and universal image quality index (UIQI). The measure of PSNR has been widely used in evaluating performance of a smoothing algorithm in the objective methodology. For a given noisy image $I$, $I(i, j, T)$ denotes the intensity of pixel $(x, y) \in I$ at iteration $T$ when an anisotropic diffusion algorithm is applied to the noisy image. $I(i, j, 0)$ is its uncorrupted ground truth. As a result, the PSNR is defined as follows:

$$\text{PSNR} = 10 \log_{10} \left( \frac{\sum_{i,j} 255^2}{\sum_{i,j} [I(i, j, 0) - I(i, j, T)]^2} \right) \text{dB}. \quad (32)$$

Recently, the measure of UIQI has been used to better evaluate image quality due to its strong ability in measuring structural distortion occurred during the image-degradation processes,[58]

$$Q = \frac{1}{M} \sum_{M=1}^{j} Q_j, \quad (33)$$

where $M$ is the total step number and $Q_j$ denotes the local quality index computed within the moving window. In this paper, a sliding window of size $8 \times 8$ is applied to estimate an entire image.

### 4.1 *General Images*

The performance of the proposed algorithm is evaluated using four $512 \times 512$ standard images with 256 gray-scale



Downloaded from SPIE Digital Library on 02 Dec 2010 to 202.114.65.9. Terms of Use: http://spiedl.org/terms

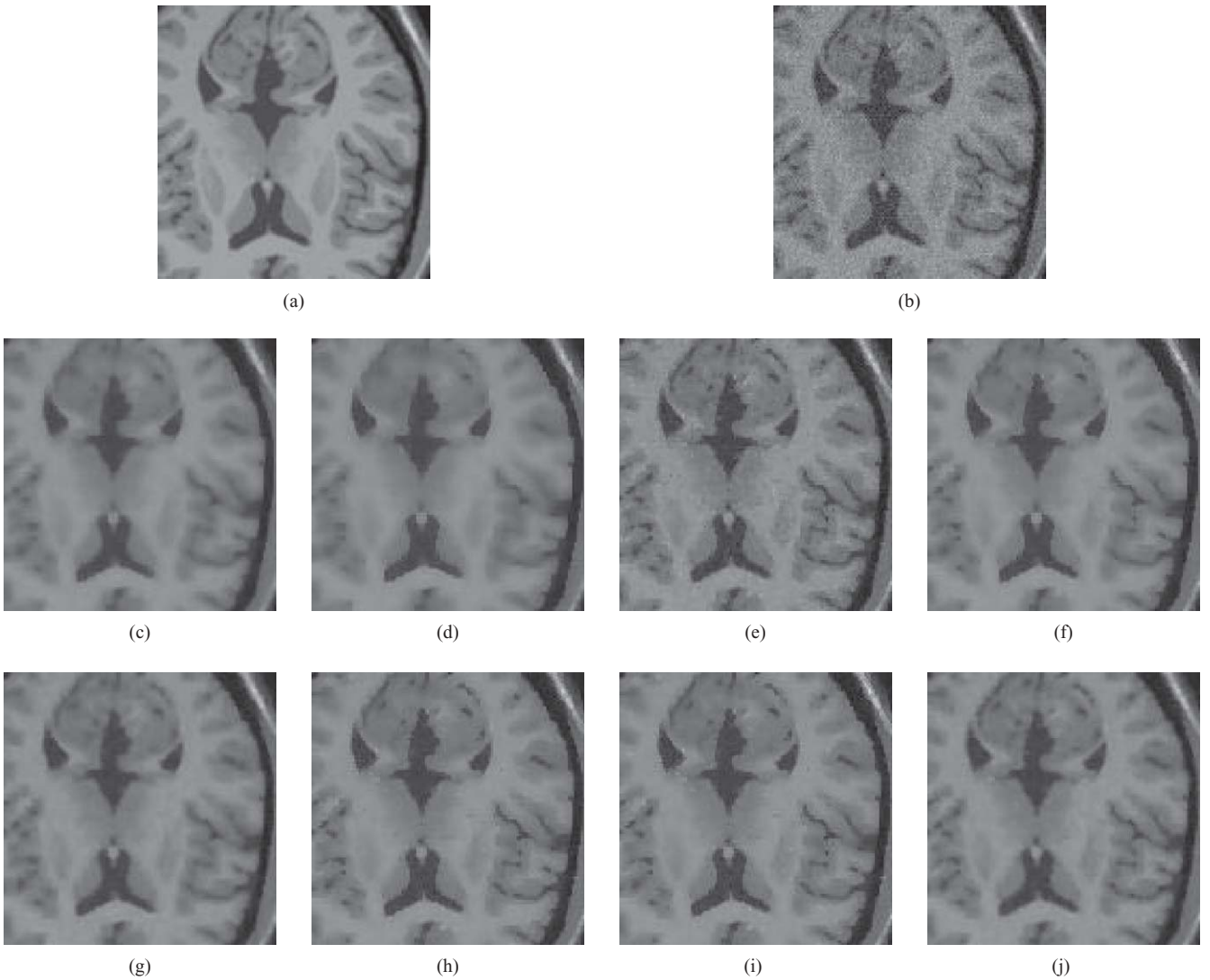


**Fig. 11** Enhanced images for the 3-D data volume of a T1-weighted MR simulated image: (a) Original MR image (slice 80), (b) corrupted MR image, (c) enhanced MR image with CAD, (d) WAD, (e) RAD, (f) MAD ($\gamma = 0.1$), (g) EED, (h) GFAB, (i) LVCFAB, and (j) RAAD ($\sigma = 0.5$, $\rho = 1$, $\delta_{\text{smooth}} = 0.2$, $\delta_{\text{detail}} = 0.6$, $\delta_{\text{edge}} = 1.2$) (10 iterations).

values. The image of Peppers is employed as an example of the piecewise-constant image. Lena and Cameraman are two examples with both textures and smooth regions. Boat is an example with different edge features. The additive Gaussian white noise with different noise levels is added to these images for performance evaluation. The PSNR and UIQI values of the four noisy images with respect to different noise variance are listed in Table 1. Two standard images and their noisy versions with noise variance 225 are displayed in Figs. 4 and 5, respectively. For clarity, only the regional enlarged portion is displayed for each image.

For comparing the visual quality of the denoised images for the six algorithms, their resultant images with respect to noise variance 225 are depicted in Figs. 6 and 7, respectively. The results yielded by CAD and WAD are depicted in Figs. 6(a) and 6(b) and Figs. 7(a) and 7(b), respectively. It should be mentioned that the CAD and WAD result in the loss of important information from the original image, though the noise is entirely removed. For RAD, a lot of noise still survives in the denoised images. In Figs. 6(d) and 7(d), very large oscillations of gradient introduced by noise cannot be fully attenuated by MAD. A better edge-preserving filtering is yielded by the EED process, and the corresponding results are shown in Figs. 6(e) and 7(e). Finally, the images produced by our algorithm are represented in Figs. 6(f) and 7(f). The noise is readily removed, and this is due to forward diffusion. Meanwhile, edge features, including most of the fine details, are sharply reproduced with the RAAD algorithm. By comparing the resultant images of RAAD to the other five classical algorithms, we note that the RAAD algorithm achieves better visual quality. The list of PSNR and UIQI values that are reported by the different algorithms, which were performed on four noisy versions of test images at different noise levels used in our experiments, are found in Table 2. Remarkably, the statistical results shown in Table 2 definitely indicate that the proposed RAAD algorithm achieves the best denoising performance among the six diffusion algorithms.

In order to appraise the effectiveness of the adaptive gradient threshold, the gradient threshold $k_f$ curves for four noisy images ($\sigma^2 = 400$) are graphically depicted in Fig. 8. It can be seen that both of the curves representing the evolution



Downloaded from SPIE Digital Library on 02 Dec 2010 to 202.114.65.9. Terms of Use: http://spiedl.org/terms

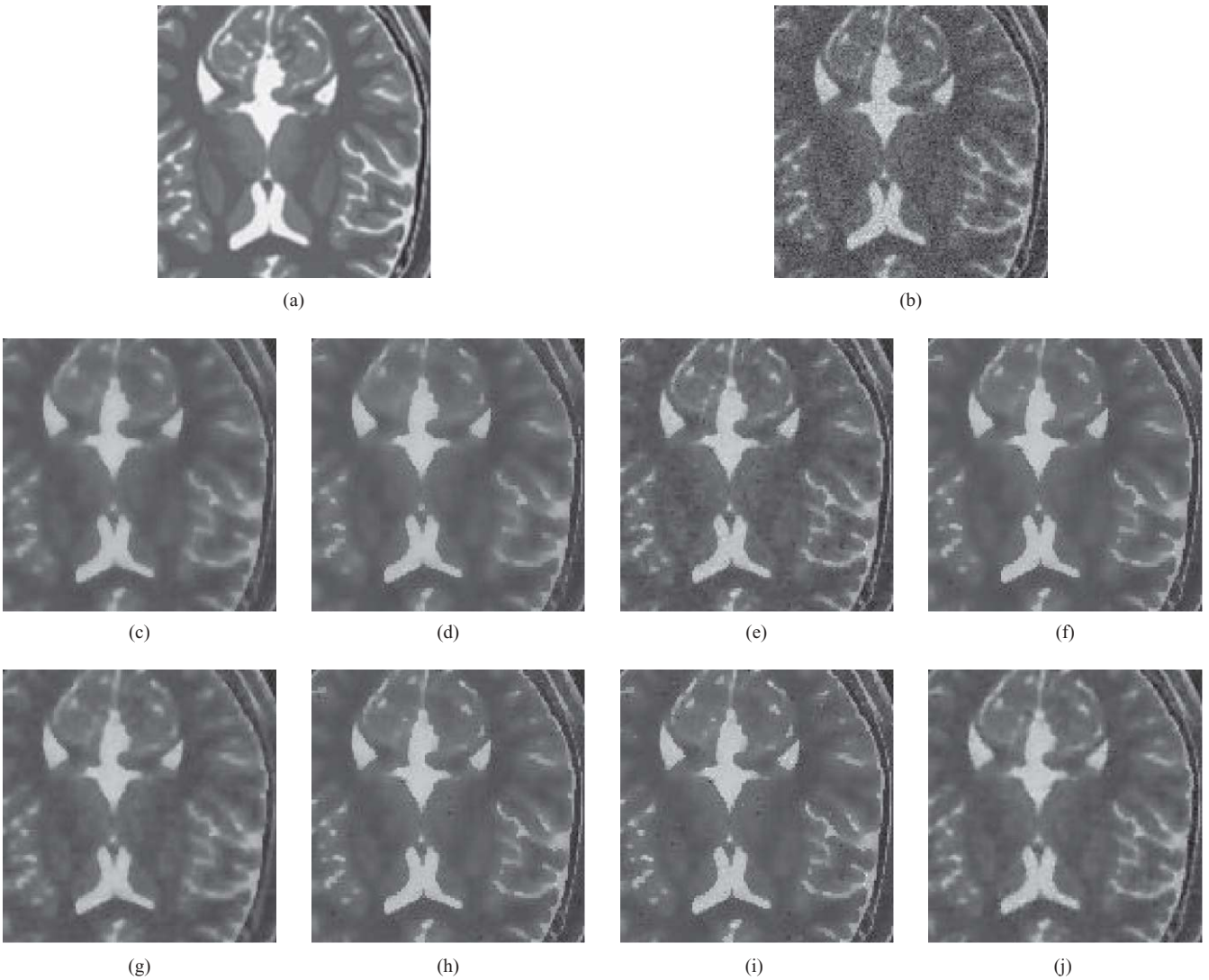


**Fig. 12** Enhanced images for the 3-D data volume of a T2-weighted MR simulated image: (a) Original MR image (slice 80), (b) corrupted MR image, (c) enhanced MR image with CAD, (d) WAD, (e) RAD, (f) MAD ($\gamma = 0.1$), (g) EED, (h) GFAB, (i) LVCFAB, and (j) RAAD ($\sigma = 0.5$, $\rho = 1$, $\delta_{\text{smooth}} = 0.2$, $\delta_{\text{detail}} = 0.6$, $\delta_{\text{edge}} = 1.2$) (10 iterations).

of this parameter share the same decreasing behavior as found in existing work, allowing lower and lower gradients to take part in the diffusing process. Moreover, after more than 20 iterations, $k_f$ decreases slower and slower and the scheme converges to a steady state where for $t \to \infty$, we get $c(|\nabla I|) \to 0$, which means that almost no diffusion is performed. The choice of an optimum threshold value has been addressed by several authors;[17,28,48,49] however, they do not explain how to determine the homogenous regions during the process. Here, an appropriate solution for automatically adapting the gradient threshold at each iteration is presented.

Second, the proposed RAAD algorithm is compared to two existing FAB diffusion algorithms: GSZ FAB diffusion[37] and LVCFAB diffusion[43] from visual quality and the PSNR and UIQI values. We present in Figs. 9 and 10 the resultant images of Lena and Boat to show the effects of the three FAB diffusion algorithms in this study. It is observed that the GSZ FAB diffusion and LVCFAB diffusion are sensitive to noise and result in developing singularities in homogeneous regions. However, the RAAD algorithm can reconcile the balance between sharpening and denoising, and exhibits the best edge-enhancing diffusion behavior. Also, from Table 3, it is evident that the RAAD algorithm is much more efficient than the GSZ FAB diffusion and LVCFAB diffusion for the four images. Because the FAB diffusion is intended for applications where the noise variance is not too large, the statistical results of three algorithms with respect to noise variance 100, 225, and 400 are shown in Table 3. Thus, we can say that the RAAD outperforms the existing FAB diffusion enhancement techniques.

### 4.2 *Medical Images*

In medical images, low SNR and CNR often degrade the information and affect several image-processing tasks, such as segmentation, classification, and registration. Therefore, it is of considerable interest to improve SNR and CNR to reduce the deterioration of image information. In this section, the proposed algorithm was implemented and tested on two 3-D magnetic resonance (MR) images,[59,60] both of which have been simulated using two sequences (T1 and T2 weighted)



Downloaded from SPIE Digital Library on 02 Dec 2010 to 202.114.65.9. Terms of Use: http://spiedl.org/terms

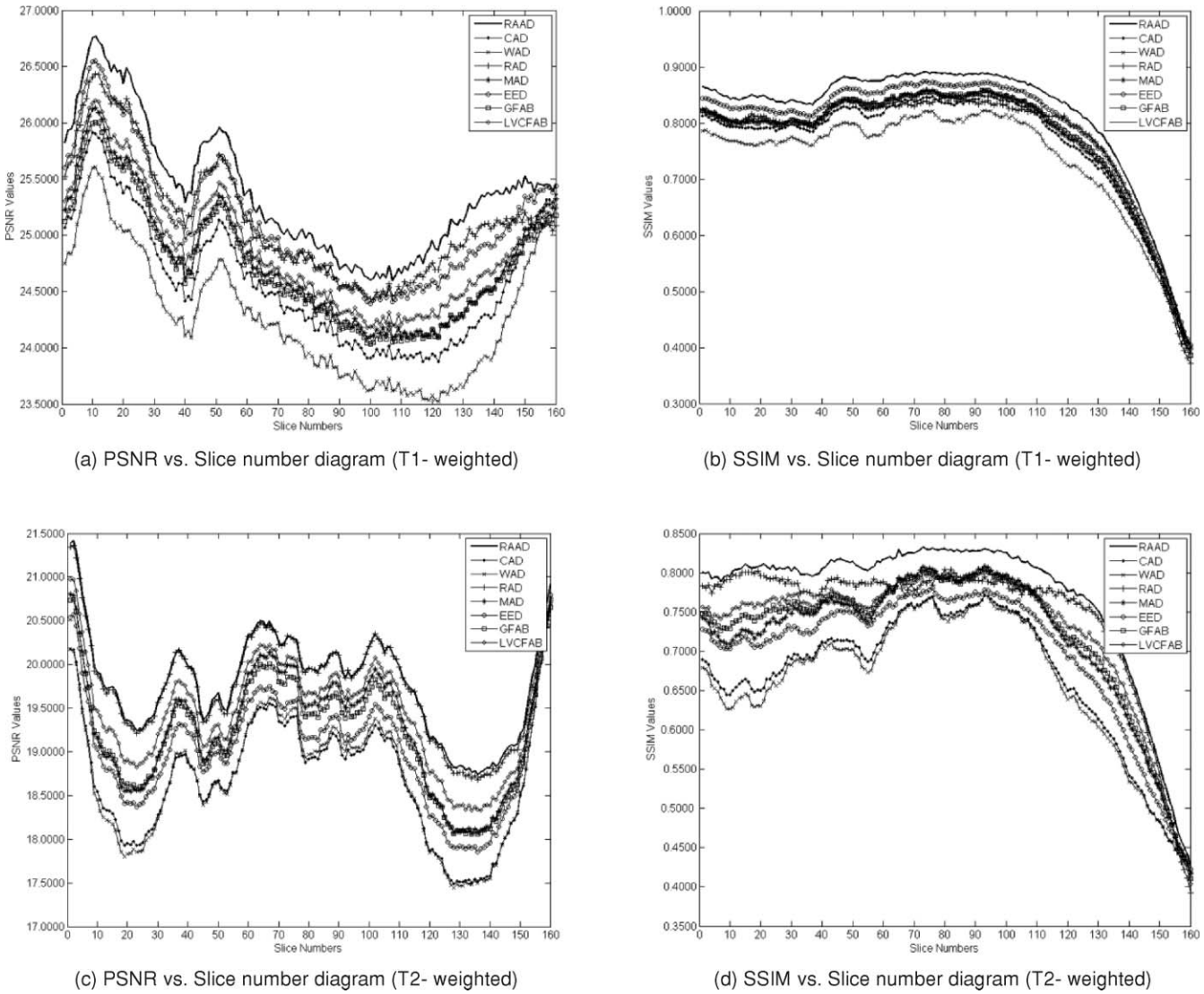


(a) PSNR vs. Slice number diagram (T1- weighted)

(b) SSIM vs. Slice number diagram (T1- weighted)

(c) PSNR vs. Slice number diagram (T2- weighted)

(d) SSIM vs. Slice number diagram (T2- weighted)

**Fig. 13** The PSNR and SSIM measures for the different diffusion algorithms at each slice of the T1- and T2-weighted MR images.

with 1 mm of slice thickness, 9% noise level, and 20% of intensity nonuniformity (downloaded from Brainweb[61]) using default acquisition parameters for each modality. These simulations are based on an anatomical model of normal brain, which can serve as the ground truth for any analysis procedure.

Figures 11 and 12 show a region of interest (ROI) from Figs. 11(a) and 12(a), and the diffusive filtered results of

**Table 1** PSNR and UIQI of the noisy standard testing images of Peppers, Lena, Cameraman, and Boat with respect to different noise variances.

| Image | Noise Variance ($\sigma^2$) | | | | | | | | | |
|---|---|---|---|---|---|---|---|---|---|---|
| | 100 | | 225 | | 400 | | 625 | | 900 | |
| | PSNR (dB) | UIQI | PSNR (dB) | UIQI | PSNR (dB) | UIQI | PSNR (dB) | UIQI | PSNR (dB) | UIQI |
| Peppers | 28.16 | 0.5411 | 24.71 | 0.4087 | 22.22 | 0.3232 | 20.31 | 0.2646 | 18.82 | 0.2237 |
| Lena | 28.14 | 0.5024 | 24.60 | 0.3891 | 22.15 | 0.3137 | 20.22 | 0.2617 | 18.70 | 0.2221 |
| Cameraman | 28.27 | 0.3806 | 24.86 | 0.3066 | 22.45 | 0.2585 | 20.56 | 0.2227 | 19.03 | 0.1945 |
| Boat | 28.13 | 0.6322 | 24.63 | 0.5031 | 22.17 | 0.4132 | 20.27 | 0.3467 | 18.73 | 0.2960 |



Downloaded from SPIE Digital Library on 02 Dec 2010 to 202.114.65.9. Terms of Use: http://spiedl.org/terms

**Table 2** PSNR and UIQI of the six diffusion algorithms for the noisy standard testing Images of Peppers, Lena, Cameraman, and Boat with respect to different noise variances.

| Scheme | Image | Noise Variance ($\sigma^2$) | | | | | | | | | |
|---|---|---|---|---|---|---|---|---|---|---|---|
| | | 100 | | 225 | | 400 | | 625 | | 900 | |
| | | PSNR (dB) | UIQI | PSNR (dB) | UIQI | PSNR (dB) | UIQI | PSNR (dB) | UIQI | PSNR (dB) | UIQI |
| CAD | Peppers | 32.93 | 0.5917 | 31.90 | 0.5681 | 30.81 | 0.5367 | 29.81 | 0.504 | 28.93 | 0.4737 |
| | Lena | 33.48 | 0.6518 | 31.16 | 0.6118 | 31.08 | 0.5733 | 30.06 | 0.5339 | 29.12 | 0.4961 |
| | Cameraman | 34.55 | 0.5819 | 32.89 | 0.5138 | 31.43 | 0.4588 | 30.06 | 0.4156 | 28.81 | 0.3806 |
| | Boat | 30.87 | 0.6252 | 30.03 | 0.6048 | 29.18 | 0.5816 | 28.31 | 0.5507 | 27.55 | 0.5252 |
| WAD | Peppers | 32.57 | 0.5771 | 31.60 | 0.5553 | 30.61 | 0.5287 | 29.67 | 0.5001 | 28.87 | 0.4719 |
| | Lena | 32.98 | 0.6345 | 31.84 | 0.6036 | 30.80 | 0.5667 | 29.87 | 0.5309 | 29.00 | 0.4959 |
| | Cameraman | 33.96 | 0.5619 | 32.51 | 0.4984 | 31.13 | 0.4487 | 29.84 | 0.4072 | 28.67 | 0.3722 |
| | Boat | 30.55 | 0.6022 | 29.73 | 0.5814 | 28.88 | 0.5579 | 28.09 | 0.5318 | 25.37 | 0.5078 |
| RAD | Peppers | 31.44 | 0.6165 | 28.27 | 0.4995 | 25.82 | 0.4118 | 23.95 | 0.3496 | 22.50 | 0.3042 |
| | Lena | 31.91 | 0.6174 | 28.36 | 0.4931 | 25.88 | 0.4095 | 23.98 | 0.3525 | 22.46 | 0.3085 |
| | Cameraman | 32.60 | 0.4944 | 28.81 | 0.3868 | 26.21 | 0.3278 | 24.23 | 0.2854 | 22.61 | 0.2538 |
| | Boat | 31.46 | 0.7036 | 28.33 | 0.6037 | 25.87 | 0.5164 | 23.98 | 0.446 | 22.42 | 0.3927 |
| MAD | Peppers | 32.66 | 0.6025 | 30.84 | 0.5538 | 28.97 | 0.493 | 27.28 | 0.4373 | 25.95 | 0.3919 |
| | Lena | 33.32 | 0.6583 | 31.19 | 0.5886 | 29.19 | 0.5137 | 27.54 | 0.4552 | 26.09 | 0.4046 |
| | Cameraman | 34.15 | 0.5809 | 31.63 | 0.4773 | 29.24 | 0.399 | 27.33 | 0.3453 | 25.77 | 0.3071 |
| | Boat | 31.25 | 0.6475 | 29.74 | 0.6103 | 28.14 | 0.5599 | 26.63 | 0.505 | 25.34 | 0.4578 |
| EED | Peppers | 33.04 | 0.613 | 31.62 | 0.5754 | 30.15 | 0.5274 | 28.88 | 0.4832 | 27.76 | 0.4447 |
| | Lena | 33.85 | 0.6702 | 32.11 | 0.6128 | 30.60 | 0.5608 | 29.23 | 0.5104 | 28.01 | 0.4656 |
| | Cameraman | 34.77 | 0.5952 | 32.72 | 0.5088 | 30.87 | 0.4508 | 29.28 | 0.4045 | 27.90 | 0.369 |
| | Boat | 31.28 | 0.6655 | 30.26 | 0.6348 | 29.14 | 0.6018 | 28.08 | 0.5613 | 27.07 | 0.5282 |
| RAAD | Peppers | 33.29 | 0.6325 | 32.06 | 0.5764 | 30.94 | 0.5395 | 29.96 | 0.5064 | 29.10 | 0.4772 |
| | Lena | 34.33 | 0.6810 | 32.53 | 0.6232 | 31.24 | 0.5749 | 30.19 | 0.5353 | 29.28 | 0.4991 |
| | Cameraman | 34.97 | 0.5994 | 33.41 | 0.5199 | 31.77 | 0.4622 | 30.36 | 0.4195 | 29.03 | 0.3859 |
| | Boat | 32.09 | 0.6886 | 30.65 | 0.6409 | 29.39 | 0.6014 | 28.39 | 0.5624 | 27.59 | 0.5314 |

this ROI using the eight diffusion algorithms. As expected, the eight algorithms remove noise present in Figs. 11(b) and 12(b), and simultaneously smooth the homogeneous regions, such as white matter. However, for RAD, GSZ FAB, and LVCFAB, noise is still remaining in the resulting images. Some structure details are not visible in the images denoised by the CAD, WAD, and MAD algorithm, though they can greatly attenuate the effect of noise. According to the visual analyses of the image quality, the results given by the EED diffusion and our algorithm are comparable because the two processes perform EED. Nevertheless, the RAAD algorithm achieves greater contrast and produces more reliable edges, which is especially useful for segmentation and classification purposes necessary in medical image applications.

In order to objectively evaluate the performances of the different diffusion algorithms on medical images, we adopt the PSNR and structural similarity (SSIM).[62] SSIM is a quality metric that measures the presence of the image structure details in the denoised images and the value of 1 is only achieved if the compared images are identical. The lowest value is zero if the images show no similarity at all. Because both the MR simulated images are 3-D data volume, we compare the PSNR and SSIM values for each slice for objective evaluation. As shown in Fig. 13, the PSNR values of the restored images achieved by our algorithm



Downloaded from SPIE Digital Library on 02 Dec 2010 to 202.114.65.9. Terms of Use: http://spiedl.org/terms

**Table 3** PSNR and UIQI of the three FAB diffusion algorithms for the noisy standard testing images of Peppers, Lena, Cameraman and Boat with respect to different noise variances.

| Scheme | Image | Noise Variance ($\sigma^2$) | | | | | |
|---|---|---|---|---|---|---|---|
| | | 100 | | 225 | | 400 | |
| | | PSNR (dB) | UIQI | PSNR (dB) | UIQI | PSNR (dB) | UIQI |
| GSZ FAB | Peppers | 31.93 | 0.592 | 29.65 | 0.5237 | 28.14 | 0.4682 |
| | Lena | 32.49 | 0.6294 | 29.86 | 0.5391 | 28.29 | 0.4833 |
| | Cameraman | 33.38 | 0.539 | 30.44 | 0.4333 | 28.56 | 0.3789 |
| | Boat | 30.92 | 0.6436 | 29.02 | 0.5963 | 27.71 | 0.5516 |
| LVCFAB | Peppers | 31.30 | 0.5883 | 27.98 | 0.4819 | 26.55 | 0.4236 |
| | Lena | 31.90 | 0.6309 | 28.21 | 0.4955 | 26.67 | 0.4337 |
| | Cameraman | 32.77 | 0.5441 | 28.68 | 0.3967 | 26.89 | 0.3413 |
| | Boat | 30.46 | 0.6487 | 27.64 | 0.5665 | 26.28 | 0.5122 |
| RAAD | Peppers | 33.29 | 0.6325 | 32.06 | 0.5764 | 30.94 | 0.5395 |
| | Lena | 34.33 | 0.6819 | 32.53 | 0.6232 | 31.24 | 0.5749 |
| | Cameraman | 35.58 | 0.5994 | 33.41 | 0.5199 | 31.77 | 0.4622 |
| | Boat | 32.40 | 0.7039 | 30.65 | 0.6488 | 29.39 | 0.6014 |

are comparable or higher than the other diffusion algorithms and the SSIM values of our algorithm are significantly higher because the RAAD scheme enhances boundary sharpness and fine structures better than other diffusion methods.

### 4.3 *Performance in Terms of Speed and Memory Requirements*

In this section, we perform comparative analysis to evaluate the various diffusion algorithms in terms of speed and memory requirements. It is necessary to declare that our code is not optimal in the sense that we made it as an intermediate step to a final code in C++. In addition, the LVCFAB scheme contains an exhausted search procedure and its speed is much slower than the other algorithms; thus, we do not report its speed and memory requirements. All the tests above were performed with a MATLAB program on MS Windows 7 running on a HP Z600 Workstation Mini Tower (Intel Xeon Quad-core 2.00 GHz, 4-GB RAM).

From Table 4, we can observe that all the diffusion algorithms occupy between 45 and 66 MB of memory space for general images ($512 \times 512$ pixels). Apparently, our algorithm requires the largest memory space. This is mainly due to the fact that our algorithm needs more intermediate variables for estimating edge orientations and discretizing the diffusion equation. Meanwhile, for MR images (160 slices, $612 \times 612$ pixels), the memory space consumed by our algorithm is comparable to that of the other algorithms (see Table 5) because the size of each slice of MR image is rather small.

It is very difficult to know which diffusion algorithm will be the fastest for a given problem. It depends on many factors, including the complexity of the problem, the number of pixels in a image, the discrete scheme for solving the diffusion equation, and the stopping time. Anisotropic diffusion in general is usually regarded as computationally heavy, due to the complexity of the formulations involved. However, we should be aware of the extremely fast growth rate of hardware power. Actually, a heavy computational burden can be solved in a couple of seconds by a personal computer. This is true for the proposed method. It can be seen from Tables 4 and 5 that the speed of our algorithm is slower than that of the other algorithms, except the EED scheme, because our algorithm contains the time-consuming procedures of region segmentation and edge orientation estimation. However, 1 s for a complete iteration on general images and 14 s for

**Table 4** Memory requirements and speed of the seven diffusion algorithms for general images (10 iterations).

| Algorithm | Memory Used (Kb) | Time Used (s) |
|---|---|---|
| CAD | 47,452 | 4.5 |
| WAD | 46,144 | 8.2 |
| RAD | 46,004 | 7.3 |
| MAD | 45,992 | 6.0 |
| EED | 64,424 | 4.3 |
| GSZ FAB | 45,880 | 11.3 |
| RAAD | 66,428 | 10.9 |



Downloaded from SPIE Digital Library on 02 Dec 2010 to 202.114.65.9. Terms of Use: http://spiedl.org/terms

**Table 5** Memory requirements and speed of the seven diffusion algorithms for MR images (10 iterations).

| Algorithm | Memory Used (Kb) | Time Used (s) |
|---|---|---|
| CAD | 34,772 | 54.6 |
| WAD | 34,664 | 114.9 |
| RAD | 34,832 | 92.9 |
| MAD | 34,596 | 72.0 |
| EED | 34,664 | 37.2 |
| GSZ FAB | 34,472 | 199.5 |
| RAAD | 35,112 | 142.0 |

MR images with 160 slices may not be real time, but indeed it is not an extreme overhead in exchange of the offered performance.

## 5 Conclusion

We have presented a novel RAAD algorithm for image enhancement and denoising. In the proposed algorithm, we first perform region-based adaptive segmentation on an image to obtain a region map that contains homogeneous, detail, and edge regions. According to the different types of regions, a variable weight is incorporated into the anisotropic diffusion PDE to adaptively encourage strong smoothing in homogeneous regions and suitable sharpening in the detail and edge regions. Then, we estimate the gradient threshold as the mean of local intensity differences on the homogeneous regions. Finally, edge-oriented patterns have been taken into account in the anisotropic diffusion discrete scheme, which allows our algorithm to smooth homogenous areas, while it performs edge enhancement better. Experimental results from our simulations show an improvement in visual effect and quantitative analyses over the state-of-the-art anisotropic diffusion schemes and demonstrate its potential for medical image applications. In the future, efforts will be concentrated on applying the algorithm to the enhancement of color images as well as establishing an adaptive stopping criterion to replace the prefixed numbers of iteration for anisotropic diffusion.

### *Acknowledgments*

This work was supported in part by the National Natural Science Foundation of China (Grants No. 40901205, No. 40771139, and No. 40930532); the Foundation of Key Laboratory of Geo-informatics of State Bureau of Surveying and Mapping under Grant 201022, the Foundation of Key Laboratory of Resources Remote Sensing & Digital Agriculture, Ministry of Agriculture (Grant No. RDA1005), the Foundation of Key Laboratory of Education Ministry for Image Processing and Intelligent Control (Grant No. 200908), the Foundation of Digital Land Key Laboratory of Jiangxi Province (Grant No. DLLJ201004), the Key Laboratory of Mine Spatial Information Technologies (Henan Polytechnic University, Henan Bureau of Surveying and Mapping), State Bureau of Surveying and Mapping (Grant KLM200902), and in the Special Fund for Basic Scientific Research of Central Colleges, China University of Geosciences, Wuhan (Grant No. CUGL090210). The authors would also like to thank the anonymous reviewers for their valuable comments and suggestions which significantly improved the quality of this paper.

### *References*

1. N. Damera-Venkata, T. D. Kite, W. S. Geisler, B. L. Evans, and A. C. Bovik, "Image quality assessment based on a degradation model," *IEEE Trans. Image Process.* **9**(4), 636–650 (2000).
2. J. S. Lee, "Digital image enhancement and noise filtering by use of local statistics," *IEEE Trans. Pattern Anal. Mach. Intell.* **2**, 165–168 (1980).
3. P. Chan and J. Lim, "One-dimensional processing for adaptive image restoration," *IEEE Trans. Acous. Speech, Signal Process.* **33**(1), 117–126 (1985).
4. D. C. C. Wang, A. H. Vagnucci, and C. C. Li, "Gradient inverse weighted smoothing scheme and the evaluation of its performance," *Comput. Graphics Image Process.* **15**(2), 167–181 (1981).
5. K. Rank and R. Unbehauen, "An adaptive recursive 2-D filter for removal of Gaussian noise in images," *IEEE Trans. Image Process.* **1**(3), 431–436 (1992).
6. C. B. Ahn, Y. C. Song, and D. J. Park, "Adaptive template filtering for signal-to-noise ratio enhancement in magnetic resonance imaging," *IEEE Trans. Med. Imaging* **18**(6), 549–556 (1999).
7. S. M. Smith and J. M. Brady, "SUSAN—a new approach to low level image processing," *Int. J. Comput. Vis.* **23**(1), 45–78 (1997).
8. T. Iijima, "Basic theory of pattern observation," in *Papers of Technical Group on Automata and Automatic Control*, IECE, Japan, Dec. 1959 (in Japanese).
9. T. Iijima, "Basic theory on normalization of a pattern (in case of typical one-dimensional pattern)," *Bull. Elec. Lab.* **26**, 368–388 (1962).
10. J. Weickert, S. Ishikawa, and A. Imiya, "Linear scale-space has first been proposed in Japan," *J. Math. Imaging Vis.* **10**(3), 237–252 (1999).
11. A. P. Witkin, "Scale-space filtering," in *Proc. of Int. Joint Conf. on Artificial Intelligence*, New York, pp. 1019–1021 (1983).
12. J. J. Koenderink, "The structure of images," *Biol. Cybern.* **50**, 363–370 (1984).
13. J. J. Koenderink and A. J. V. Doorn, "Generic neighborhood operators," *IEEE Trans. Pattern Anal. Mach. Intell.* **14**(6), 597–605 (1992).
14. T. Lindeberg, "Feature detection with automatic scale selection," *Int. J. Comput. Vis.* **30**(2), 77–116 (1998).
15. A. L. Yuille and T. Poggio, "Scaling theorems for zero-crossings," *IEEE Trans. Pattern Anal. Mach. Intell.* **8**(1), 15–25 (1986).
16. J. Babaud, A. P. Witkin, M. Baudin, and R. O. Duda, "Uniqueness of the Gaussian kernel for scale-space filtering," *IEEE Trans. Pattern Anal. Mach. Intell.* **8**(1), 26–33 (1986).
17. P. Perona and J. Malik, "Scale-space and edge detection using anisotropic diffusion," *IEEE Trans. Pattern Anal. Mach. Intell.* **12**(7), 629–639 (1990).
18. F. Catte, P. L. Lions, J. M. Morel, and T. Coll, "Image selective smoothing and edge detection by nonlinear diffusion," *SIAM J.Numer. Anal.*, **29**(1), 182–193 (1992).
19. L. Alvarez, P. L. Lions, and J. M. Morel, "Image selective smoothing and edge detection by nonlinear diffusion," *SIAM J. Numer. Anal.*, **29**(3), 845–866 (1992).
20. G. Gerig, O. Kubler, R. Kikinis, and F. A. Jolesz, "Nonlinear anisotropic filtering of MRI data," *IEEE Trans. Med. Imaging* **11**(2) 221–232 (1992).
21. M. Nitzberg, and T. Shiota, "Nonlinear image filtering with edge and corner enhancement," *IEEE Trans. Pattern Anal. Mach. Intell.* **14**(8), 826–833 (1992).
22. R. T. Whitaker and S. M. Pizer, "A multi-scale approach to nonuniform diffusion," *Comput. Vis. Graphics Image Process. Image Understand.* **57**, 99–110 (1993).
23. L. Alvarez and L. Mazorra, "Signal and image restoration using shock filters and anisotropic diffusion," *SIAM J. Numer. Anal.* **31**(2), 590–605 (1994).
24. X. Li and T. Chen, "Nonlinear diffusion with multiple edginess thresholds," *Pattern Recogn.* **27**(8), 1029–1037 (1994).
25. J. Weickert, "Theoretical foundations of anisotropic diffusion in image processing," *Computing* **11**, 221–236 (1996).
26. B. Fischl and E. L. Schwartz, "Learning an integral equation approximation to nonlinear anisotropic diffusion in image processing," *IEEE Trans. Pattern Anal. Mach. Intell.* **19**(4), 342–352 (1997).
27. S. T. Acton, "Multigrid anisotropic diffusion," *IEEE Trans. Image Process.* **7**(3), 280–291 (1998).
28. M. J. Black, G. Sapiro, D. H. Marimont, and D. Heeger, "Robust anisotropic diffusion," *IEEE Trans. Image Process.* **7**(3), 421–432 (1998).
29. J. Weickert, *Anisotropic Diffusion in Image Processing*, BG Teubner Stuttgart, (1998).



Downloaded from SPIE Digital Library on 02 Dec 2010 to 202.114.65.9. Terms of Use: http://spiedl.org/terms

30. J. Weickert, B. M. T. H. Romeny, and M. A. Viergever, "Efficient and reliable schemes for nonlinear diffusion filtering," *IEEE Trans. Image Process.* **7**(3), 398–410 (1998).
31. B. Fischl and E. L. Schwartz, "Adaptive nonlocal filtering: a fast alternative to anisotropic diffusion for image enhancement," *IEEE Trans. Pattern Anal. Mach. Intell.* **21**(1), 42–48 (1999).
32. J. Monteil and A. Beghdadi, "A new interpretation of the nonlinear anisotropic diffusion for image enhancement," *IEEE Trans. Pattern Anal. Mach. Intell.* **21**(9), 940–946 (1999).
33. S. T. Acton, "Locally monotonic diffusion," *IEEE Trans. Signal Process.* **48**(5), 1379–1389 (2000).
34. I. Pollak, A. S. Wilsky, and H. Krim, "Image segmentation and edge enhancement with stabilized inverse diffusion equations," *IEEE Trans. Image Process.* **9**(2), 256–266 (2000).
35. G. Sapiro, *Geometric Partial Differential Equations and Image Analysis*, Cambridge University Press, Cambridge, England (2001).
36. G. Aubert and P. Kornprobst, *Mathematical Problems in Image Processing: Partial Differential Equations and the Calculus of Variations*, Springer-Verlag, Berlin (2002).
37. G. Gilboa, N. Sochen, and Y. Y. Zeevi, "Forward-and-backward diffusion processes for adaptive image enhancement and denoising," *IEEE Trans. Image Process.* **11**(7), 689–703 (2002).
38. P. Mrázek and M. Navara "Selection of optimal stopping time for nonlinear diffusion filtering," *Int. J. Comput. Vis.* **52**(2/3), 189–203 (2003).
39. G. Gilboa and N. S. Y. Y. Zeevi, "Image enhancement and denoising by complex diffusion processes," *IEEE Trans. Pattern Anal. Mach. Intell.* **25**(8), 1020–1036 (2004).
40. S. Young-Chul and C. Doo-Hyun, "Scale-based image enhancement using modified anisotropic diffusion filter," *Opt. Eng.* **43**(9), 2094–2099 (2004).
41. D. Tschumperle and R. Deriche, "Vector-valued image regularization with PDEs: a common framework for different applications," *IEEE Trans. Pattern Anal. Mach. Intell.* **27**(4), 1–12 (2005).
42. J. M. Duarte-Carvajalino, P. E. Castillo, and M. Velez-Reyes, "Comparative study of semi-implicit schemes for nonlinear diffusion in hyperspectral imagery," *IEEE Trans. Image Process.* **16**(5), 1303–1314 (2007).
43. Y. Wang, L. Zhang, and P. Li, "Local varianced-controlled forward-and-backward diffusion for image enhancement and noise reduction," *IEEE Trans. Image Process.* **16**(7), 1854–1864 (2007).
44. J. Zhong and H. Sun, "Wavelet–based multiscale anisotropic diffusion with adaptive statistical analysis for image restoration," *IEEE Trans. Circ. Syst.* **55**(9), 2716–2725 (2008).
45. Y. Wang, R. Niu, and X. Yu, "Anisotropic diffusion for hyperspectral imagery enhancement," *IEEE Sens. J.* **10**(3), 469–477 (2010).
46. Y. Wang, R. Niu, X. Yu, L. Zhang, and H. Shen, "Image restoration and enhancement based on tunable forward-and-backward diffusion," *Opt. Eng.* **49**(5), 057004 (2010).
47. C. Harris and M. Stephens, "A combined corner and edge detector," in *Proc. of 4th Alvey Vision Conf.*, pp. 147–152 (1988).
48. F. Voci, S. Eiho, N. Sugimoto, and H. Sekibuchi, "Estimating the gradient in the Perona-Malik equation," *IEEE Signal Process. Mag.* **21**(3), 39–65 (2004).
49. M. J. Black and G. Sapiro, "Edges as outliers: anisotropic smoothing using local image statistics," in *Proc. of Scale-Space Conf.*, Berlin, pp. 259–270 (1999).
50. F. Torkamani-Azar and K. E. Tait, "Image recovery using the anisotropic diffusion equation," *IEEE Trans. Image Process.* **5**(11), 1573–1578 (1996).
51. R. Whitaker and G. Gerig, *Geometrically-Driven Diffusion in Computer Vision*, Kluwer, Norwell, MA (1994).
52. J. Weickert, "Anisotropic diffusion in image Process," Ph.D. thesis, Dept. of Mathematics, University of Kaiserslautern, P.O. Box 3049, 67653 Kaiserslautern, Germany (1996).
53. J. Weickert, "Coherence-enhancing diffusion filtering," *Int. J. Comput. Vis.* **31**(2–3), 111–127 (1999).
54. W. K. Pratt, *Digital Image Processing,* 3rd ed., Wiley, Hoboken, NJ (2001).
55. B. Choi, S. D. Kim, and J. B. Ra, "Region-based super-resolution using adaptive diffusion regularization," *Opt. Eng.* **47**(2), 027006 (2008).
56. E. Ardizzone, R. Pirrone, R. Gallea, and O. Gambino, "Noise filtering using edge-driven adaptive anisotropic diffusion," in *Proc. of IEEE Int. Symp. on Computer-Based Medical Systems (CBMS 2008)*, New Mexico, pp. 29–34 (2008).
57. K. Chen, "Adaptive smoothing via contextual and local discontinuities," *IEEE Trans. Pattern Anal. Mach. Intell.* **27**(10), 1552–1567 (2005).
58. Z. Wang and A. C. Bovik, "A universal image quality index," *IEEE Signal Process. Lett.* **9**(3), 81–84 (2002).
59. R. Kwan, A. Evans, and G. Pike, "An extensible MRI simulator for post-processing evaluation," *Visualization Biomed. Comput.* **1131**, 135–140 (1996).
60. R. K. S. Kwan, A. C. Evans, and G. B. Pike, "MRI simulation-based evaluation of image-processing and classification methods," *IEEE Trans. Med. Imaging* **18**(11), 1085–1097 (1999).
61. Brainweb: http://mouldy.bic.mni.mcgill.ca/brainweb/.
62. Z. Wang, A. C. Bovik, H. R. Sheikh, and E. P. Simoncelli, "Image quality assessment: from error visibility to structural similarity," *IEEE Trans. Image Process.* **13**(4), 600–612 (2004).


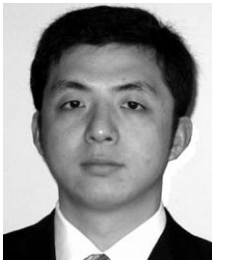

**Yi Wang** received his BS, MS, and PhD in photogrammetry and remote sensing from Wuhan University, Wuhan, in 2002, 2004, and 2007, respectively. He is currently an associate professor with the Institute of Geophysics and Geomatics, China University Geosciences. His research interests include remote sensing image processing using partial differential equations and, particularly, pattern recognition.

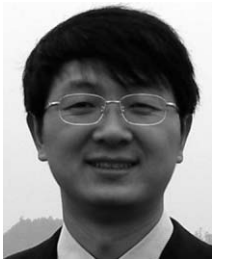

**Ruiqing Niu** received his BS, MS, and PhD from China University of Geosciences, Wuhan, in 1992, 2001, and 2005, respectively. He is currently an associate professor with the Institute of Geophysics and Geomatics, China University of Geosciences. His research interests include geovisualization, environmental remote sensing, and geological remote sensing.

**Liangpei Zhang** received his BS degree in physics from Hunan Normal University, ChangSha, China, in 1982, his MS degree in optics from the Xi'an Institute of Optics and Precision Mechanics of Chinese Academy of Sciences, Xi'an, China, in 1988, and his PhD degree in photogrammetry and remote sensing from Wuhan University, Wuhan, China, in 1998. He is currently with the State Key Laboratory of Information Engineering in Surveying, Mapping and Remote Sensing, Wuhan University, as the head of the Remote Sensing Division. He is also a "Chang-Jiang Scholar" Chair Professor appointed by the Ministry of Education, China. He has more than 200 research papers and 5 patents. He is now Principal Scientist for the China State Key Basic Research Project (2011–2016) appointed by the Ministry of National Science and Technology of China to lead the remote sensing program in China. His research interests include hyperspectral remote sensing, high resolution remote sensing, image processing and artificial intelligence. He regularly serves as a Co-Chair of the series SPIE Conferences on Multispectral Image Processing and Pattern Recognition (MIPPR), Conference on Asia Remote Sensing, and many other conferences. He edits several conference proceedings, issues, and the Geoinformatics Symposiums. He also serves as an Associate Editor of International Journal of Ambient Computing and Intelligence (IJACI), International Journal of Image and Graphics, Journal of Geo-spatial Information Science, and the Journal of Remote Sensing. He is Fellow of IEE, Executive Member (Board of Governor) of the China National Committee of International Geosphere-Biosphere Programme, Executive Member for the China Society of Image and Graphics, and others.

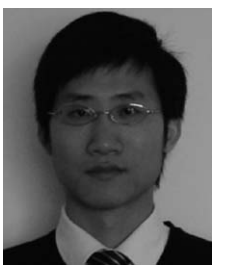

**Huanfeng Shen** received his BS, MS, and PhD in photogrammetry and remote sensing from Wuhan University, Wuhan, in 2002, 2004, and 2007, respectively. He is currently an associate professor at the School of Resource and Environmental Science, Wuhan University. His main research interest is image superresolution enhancement.



Downloaded from SPIE Digital Library on 02 Dec 2010 to 202.114.65.9. Terms of Use: http://spiedl.org/terms